Published in final edited form as:
Laser Photon Rev. 2011 July ; 5(4): . doi:10.1002/lpor.201000027.

Multimodal Nonlinear Optical Microscopy

Shuhua Yue, **Mikhail N. Slipchenko**, and **Ji-Xin Cheng***
Weldon School of Biomedical Engineering, Purdue University, West Lafayette, IN 47907

Abstract

Because each nonlinear optical (NLO) imaging modality is sensitive to specific molecules or structures, multimodal NLO imaging capitalizes the potential of NLO microscopy for studies of complex biological tissues. The coupling of multiphoton fluorescence, second harmonic generation, and coherent anti-Stokes Raman scattering (CARS) has allowed investigation of a broad range of biological questions concerning lipid metabolism, cancer development, cardiovascular disease, and skin biology. Moreover, recent research shows the great potential of using CARS microscope as a platform to develop more advanced NLO modalities such as electronic-resonance-enhanced four-wave mixing, stimulated Raman scattering, and pump-probe microscopy. This article reviews the various approaches developed for realization of multimodal NLO imaging as well as developments of new NLO modalities on a CARS microscope. Applications to various aspects of biological and biomedical research are discussed.

Keywords

CARS; multimodal; NLO microscopy; biomedical; nanomaterial; TPEF; SHG; confocal Raman; SRS; FWM; transient absorption; photothermal

1. Introduction

Coupling of nonlinear optics and scanning microscopy has generated a panel of imaging tools for biology and materials research. The nonlinear optical (NLO) microscopy family can be categorized into one-beam and two-beam modalities. The one-beam modality includes multiphoton fluorescence (for reviews see [1, 2]), second harmonic generation (SHG) (for a review see [3]) and third harmonic generation (THG) [4] microscopy. The two-beam modality includes coherent anti-Stokes Raman scattering (CARS) (for reviews see [5–10]), four-wave mixing (FWM) (for review see [11]), stimulated Raman scattering (SRS) [12–17], pump-probe (for reviews see [18, 19]), and photothermal microscopy (for review see [20, 21]). Because each NLO imaging modality is sensitive to specific molecules or structures, multimodal NLO imaging capitalizes the potential of NLO microscopy for studies of complex tissue samples. The coupling of multiphoton fluorescence, SHG, and THG has led to many biological applications (for examples see [22–26]). In this article, we review the development and applications of multimodal NLO microscopy achieved through a CARS microscopy platform. Based on studies by our lab and other research groups, we show that the capability of CARS microscopy is much enhanced by incorporation of other NLO imaging modalities and microspectroscopy channels. Moreover, we show that CARS microscope provides a basic platform for building new modalities such as FWM, SRS, and transient absorption microscopy. The rest of our paper is organized as follows. Section 2 presents an overview of NLO processes used for imaging. Section 3 discusses the experimental approaches for multimodal imaging and spectral analysis on a CARS

*Corresponding author: jcheng@purdue.edu.

microscope. Section 4 review the various applications enabled by multimodal NLO imaging. Finally we present an outlook.

2. Overview of NLO modalities

Multimodal NLO microscope, which integrates multiple imaging modalities on the same platform, allows visualization of different endogenous and exogenous structures in cells and tissues. Fig. 1 shows the imaging modalities that have been demonstrated. These imaging modalities include well-established modalities such as CARS [27], two-photon excited fluorescence (TPEF) [28], SHG [3], and THG [29, 30] microscopy, and modalities developed for characterization of nanostructures, such as two-photon luminescence (TPL) and three-photon luminescence (3PL), and FWM microscopy. Recently, several new two-beam modalities have been developed, including stimulated Raman scattering (SRS), pump-probe, and photothermal microscopy. Below we give a concise description of the NLO processes responsible for contrast mechanisms in the above mentioned modalities. Detailed discussion of major NLO modalities can be found in a recent book entitled *Handbook of Biomedical Nonlinear Optical Microscopy* [31].

2.1 Coherent anti-Stokes Raman scattering (CARS)

CARS is a four-wave mixing process in which a pump beam (ω_p) and a Stokes beam (ω_s) interact with a sample to generate a signal at the anti-Stokes frequency $\omega_{as} = 2\omega_p - \omega_s$ [32]. The CARS signal arises from the nonlinear polarization induced by pump and Stokes beams due to the third-order susceptibility of the sample. The third-order susceptibility consists of a non-resonant part, which is independent of $\omega_p - \omega_s$ frequency, and a resonant part, which depends on the $\omega_p - \omega_s$ frequency. Because CARS signal can be significantly enhanced by molecular vibrations when $\omega_p - \omega_s$ is close to the vibrational frequency of a chemical bond, the CARS microscopy allows label-free and chemically selective imaging as discussed in multiple reviews [5–10].

2.2 Two-photon excited fluorescence (TPEF)

In TPEF, the target molecule absorbs two photons to reach an excited electronic state and then emits a single-fluorescence photon of higher energy than either of the incident photons [34]. Compared to one-photon fluorescence, TPEF microscopy, first demonstrated in 1990 by Denk *et al.* [28], provides inherent three-dimensional (3-D) resolution with tightly focused excitation. The small excitation volume of TPEF greatly reduces overall specimen photodamage as well as fluorophores photobleaching. Moreover, the use of near infrared (NIR) excitation for TPEF allows deeper penetration into the imaged tissues. Owing to the availability of fluorescent labels, TPEF has become the most widely used NLO imaging modality and a potent tool for biological studies [1, 2].

2.3 Sum frequency generation (SFG) and second harmonic generation (SHG)

SFG is a second-order NLO process in which two incident photons are converted to one emission photon with energy exactly equal to the sum of the excitation photons [32]. SFG is selectively sensitive to non-centrosymmetric structures. Ji *et al.* constructed the first optically active SFG microscope, which allows chirality-sensitive, 3-D sectional images with submicron spatial resolution [35]. SHG is a special case of SFG in which the two excitation photons are degenerate. SHG microscopy has been shown to be a sensitive probe for biomolecular arrays in cells, tissues, and organisms (for reviews see [3, 36]). In addition, protein crystals have been selectively detected by SHG microscopy [37]. Moreover, SHG signal has been used for nanoparticle tracking in vivo [38, 39].

2.4 Third harmonic generation (THG)

THG is a third order NLO process and unlike SHG, is not limited to non-centrosymmetric structures. THG requires three photons in order to generate one at a tripled frequency. Under tight focusing conditions, the THG signal from a homogeneous, normally dispersive medium vanishes as a consequence of the Gouy phase shift experienced by the excitation beam near focus [32, 40]. This effect makes THG sensitive to interfaces, as first shown by Tsang *et al.* in 1995 [41]. Based on THG signal from interfaces, Barad *et al.* [29] developed a THG microscope for visualization of interfaces in transparent materials. Several groups have extended the application of THG microscopy to biological samples [4, 22, 23, 36, 42, 43]. THG signal from nanoparticles can be resonantly enhanced by surface plasmon resonances, which facilitate imaging of nanoparticles and make the nanoparticles potential biomarkers as first shown by Yelin *et al.* [44].

2.5 Multiphoton luminescence

Metal nanoparticles are capable of photoluminescence and, unlike single molecules, are photostable under long illumination, which makes them excellent optical imaging agents. Multiphoton luminescence is attractive owing to the brightness and intrinsic 3-D spatial resolution. Multiphoton luminescence from metals is considered to follow the same scenario as single photon luminescence which is believed to happen in three-step process [45]: (i) excitation of electron from d- to sp- band to generate electron-hole pairs; (ii) interaction of electrons and holes with lattice on picosecond (ps) time scale with partial energy transfer to phonons; (iii) electron-hole recombination resulting in photoemission. The multiphoton luminescence from metals was first observed by Chen *et al.* in 1981 [46] and further explored in 1986 by Boyd *et al.* [47], who showed that in case of rough metal surfaces the weak multiphoton luminescence signal can be amplified due to a resonant coupling with localized surface plasmons. As first demonstrated by Yelin *et al.*, the enhanced multiphoton luminescence allowed visualization of gold nanoparticles in cellular environment [44]. The strong two-photon luminescence has been widely used to visualize a variety of gold nanostructures, including gold nanoparticles [48], gold nanorods (NRs) [49], and gold nanoshells [50].

2.6 Electronic-resonance-enhanced four wave mixing (FWM)

Unlike the CARS modality that generates contrast based on vibrational resonances, the electronic-resonance-enhanced FWM modality is based on the electronic properties of a material. When one of the beams or combination of beams are resonant with electronic transitions of the material (see Fig. 1 for two-photon resonance FWM), the FWM signal can be significantly enhanced. Because the FWM signal from nanomaterials can be electronically enhanced by several orders of magnitude, it allows visualization of single nanostructures, such as gold NRs [51], gold nanowires (NWs) [52, 53], and single-walled carbon nanotubes [54] (for a review, see [11]).

2.7 Stimulated Raman scattering (SRS)

SRS was first observed by Woodbury and Ng in 1962 [55] and by Jones and Stoicheff in 1964 [56]. Stimulated Raman spectroscopy utilizing two cw laser beams and phase-sensitive detection, was first reported in 1977 by Owyoung and Jones [57]. In stimulated Raman gain (SRG) or Raman loss (SRL), the pump (Stokes) beam intensity is decreased (or increased) via the coherent Raman process (see Fig. 1 for SRG). The advantages of SRS over CARS lies in that the SRS signal is completely free of the non-resonant background and the spectral profile is identical to the spontaneous Raman spectrum. In microscopy, the modulations of pump and Stokes beam intensities due to the SRS process are usually very small ($D I/I < 10^{-4}$) as calculated for experimental imaging conditions [58]. Therefore,

modulation of the excitation beam and phase-sensitive detection method are needed to pick the signal out of the laser noise. High-speed SRS microscopy has been recently demonstrated [12–17] and applied to vibrational imaging of tablets and biomass [59, 60].

2.8 Transient absorption

Many molecules found in biological samples do not generate fluorescence due to fast non-radiative decay of electronically excited state. These dark molecules still can be probed using pump-probe transient absorption techniques as discussed in recent review by Ye *et al.* [18]. In the pump-probe modality the pump beam induces a transient electronic absorption in the sample. This change in electronic state is then sensed by the probe beam. By varying time delay between pump and probe pulses, the information on excited state dynamics can be deduced. Pump-probe microscopy has been used in transient absorption imaging of hemoglobin [61, 62], skin pigments [63–65], and nanostructures [19, 66, 67]. Particularly, Jung *et al.* used transient absorption to distinguish semiconducting and metallic single-walled carbon nanotubes (SWNTs) [68]. Min *et al.* demonstrated stimulated emission microscopy for visualizing non-fluorescent chromoproteins and chromogenic reporter for gene expression [69].

2.9 Photothermal effect

In condensed phase, upon excitation of molecules the energy is fast distributed over many vibrational modes and eventually transferred into the surrounding medium, which corresponds to a local heating. The heat causes thermal expansion and subsequent change in refractive index of the sample. This process under focusing conditions manifests itself as a thermal lens effect. In microscopy, the thermal lens caused by the pump beam affects the divergence of the probe beam as demonstrated by Harada *et al.* in 1993 [70]. For nano-sized absorbers, photothermal heterodyne microscopy has been first demonstrated by Boyer *et al.* [71]. This method is based on the refractive index change of the medium surrounding the laser-irradiated nanostructures.

3. Experimental realization of multimodal NLO imaging on a CARS microscope

3.1 CARS microscope

The development of CARS microscopy has been extensively reviewed [5–8, 10, 31, 33, 72–75]. Here we focus on the developments towards multimodal imaging. The block diagram of a modern high-speed, multifunctional CARS microscope is shown in Fig. 2. The key technological steps, which opened CARS microscopy for biomedical applications over the past decade, include: (1) Collinear beam geometry, which significantly simplifies the beam configuration; (2) Laser scanning on a confocal platform, which allows fast CARS imaging with speed as high as video rate; (3) Backward (epi) detection, which enables CARS imaging of sub-wavelength features and tissues in live animals; (4) Development of robust laser sources.

Over the past decade, several generations of laser systems have been developed for CARS microscopy. It is important to note that the choice of pulse duration for CARS microscopy is a compromise between CARS signal strength and specificity as first shown analytically by Cheng *et al.* [33]. Shorter broadband pulses produce stronger signal but also stronger non-resonant background, while longer pulses generate lower signal but better spectral resolution and specificity. High-speed CARS imaging was first demonstrated with ps lasers [76, 77]. Although ps pulse excitation gives better contrast, the femtosecond (fs) laser sources have higher peak power that is required to generate strong NLO signals for one-beam modalities

[78]. Towards the goal of coupling CARS with widely used multiphoton fluorescence microscopes, Chen *et al.* [78] and Pegoraro *et al.* [73] demonstrated multimodal NLO imaging on a CARS microscope with fs laser pulses. Rocha-Mendoza *et al.* [79] applied spectral focusing of broadband fs pulses [80] to achieve high spectral resolution in CARS imaging. More recently, Lu *et al.* demonstrated that a unique dual 4-f paired-gratings spectral filtering of a fs laser could easily switch between ps and fs pulse duration, which rendered high contrast CARS imaging and high quality multiphoton imaging, respectively [81]. Performances of CARS microscopy using ps and fs laser systems were recently compared by Svedberg *et al.* [82]. In general, fs system can provide the same CARS intensity with about 60 times lower excitation powers compared to the ps system [82]. Meanwhile, it should be emphasized that the spectral resolution in fs CARS is much reduced and this method is suitable for isolated Raman bands.

A modern CARS microscope can be operated using either ps or fs laser systems, including two synchronized Ti:sapphire lasers [33, 83], optical parametric oscillators (OPOs) pumped with solid state lasers [77, 78, 84, 85] or with fiber lasers [86], several non-linear fiber based systems [87–92] and an Er:fiber based all fiber system [93]. The Ti:sapphire lasers provide the capability of wide tuning and availability of ps and fs configuration in the same cavity. The drawback of this system is the timing jitter of electronic synchronization. The OPO-based laser systems completely resolve the timing jitter problem, because the OPO pulse train is inherently synchronized with pump laser pulse train. A remaining drawback of the free space lasers and OPOs is their high cost and large volume. Therefore, fiber-based solutions are attractive because of less expensive and more compact laser sources. Currently, the average power of the Stokes beam for fiber-based systems is limited to about 10 mW. A relatively large power for the pump beam of shorter wavelength is then necessary to achieve high speed CARS imaging. Such configurations however may increase the possibility of tissue damage.

3.2 Coupling CARS with TPEF and SHG

A challenge for multimodal imaging is simultaneous acquisition of various NLO signals in a convenient way. Such challenge can be dealt with by utilizing the coherence properties of the NLO signals. Due to the coherent addition, majority of the CARS signal goes forward and is highly directional. As shown by Cheng *et al*. [94] and Volkmer *et al*. [95], the forward CARS (F-CARS) signal is highly directional and can be efficiently collected by a NA=0.55 air condenser. Because the fluorescence signal is spectrally broad and incoherent, it is negligible after the narrow bandpass CARS filters and the air condenser in the forward channel. Instead, the backward fluorescence can be effectively collected by the laser-focusing objective with high numerical aperture (NA). Therefore, one is able to record the forward CARS signal and backward TPEF signal simultaneously using the two external photomultiplier tubes (PMTs), as shown in Fig. 2.

Due to the Gouy phase shift, the forward SHG signal is deflected from the optical axis [96] and is fairly weak if a low-NA air condenser is used. Meanwhile a significant amount of SHG photons from either collagen fibrils or protein crystals are back scattered [37, 97]. Thus, the forward CARS and backward SHG signals can be simultaneously detected by using bandpass filters and the external PMTs. Because the TPEF signal is red-shifted from the SHG signal, the SHG and TPEF signals can be spectrally separated. Huff *et al*. [98] demonstrated that with two backward detectors, dichroic mirror and appropriate bandpass filters SHG (SFG) and TPEF signals can be detected simultaneously with forward CARS signal.

3.3 Implementation of THG modality

The optical properties of tissues, sensitivity of detectors, and transmission of optics together restrict the THG signal wavelength to be longer than 350 nm. Fortunately, CARS requires no electronic resonance, and thus NIR excitation wavelengths above 1.0 μm can be used, such as the 1064 nm beam provided by high-Q laser. Such configuration opens the opportunity to couple CARS with THG imaging. Because THG signal depends on the cube of excitation beam intensity, fs laser system is usually required to produce high enough peak power to generate strong THG signal. Using fs pulses, Chen *et al.* [78] demonstrated the use of the second harmonic of the OPO idler beam at 1018 nm as the Stokes beam for CARS, and the OPO signal beam at 1290 nm for THG imaging on the same platform. It is also important to note that THG signal from interfaces is highly directional and is generated in the forward direction, as shown by Cheng *et al.* [40].

3.4 Implementation of two-photon luminescence (TPL) and three-photon luminescence (3PL)

Implementation of TPL modality is similar to that of TPEF, because TPL has the same excitation and emission characteristics as TPEF. Using a femtosecond Ti:sapphire laser, Wang *et al*. reported TPL imaging of single gold NRs *in vitro* and *in vivo* [49]. Emission spectrum of 3PL is similar to that of TPL, but 3PL needs longer excitation wavelength. Tong *et al.* have recently used a femtosecond OPO to implement 3PL imaging of gold-silver nanocages [99].

3.5 Implementation of electronic-resonance-enhanced FWM modality

The electronic-resonance-enhanced FWM is a two-beam modality with emission similar to CARS, however unlike CARS it is originated from broad electronic and/or plasmonic resonances, which usually have dephasing time on the fs time scale [100]. Therefore, fs lasers are preferred over ps ones for optimizing the efficiency of the electronic-resonance-enhanced FWM process, as has been demonstrated by Jung *et al.* [51] and discussed in the recent review by Wang *et al.*[11]. A single-beam near-degenerate FWM microscopy has been demonstrated by Min *et al.* [101] and applied to ultrasensitive detection of chromophores and hemoglobin.

3.6 Implementation of SRS modality

Because SRS and CARS occur simultaneously, it is natural to implement SRS imaging on a CARS microscope. The SRS signal originates from an intensity gain of the Stokes beam (SRG setup) or an intensity loss of the pump beam (SRL setup). The small change in intensity of the detected beam due to SRS process is buried in the noise, and so phase-sensitive detection via a lock-in amplifier is required to recover the signal. For high-speed detection of SRG signal, the intensity of pump beam is modulated, usually at MHz frequency, and the intensity of Stokes beam is detected with large area photodiode (see Fig. 2). As in any heterodyne detected processes, the noise in the detected beam limits the ultimate sensitivity. Freudiger *et al.* [14] and Nandakumar *et al.* [13, 15] have achieved high-speed SRS microscopy by using high-frequency modulation (>1 MHz) that avoids the low-frequency laser noise. Ozeki *et al.* compared the signal-to-noise ratio in CARS and SRS [12].

It is important to understand that the detection strategy is different for these modalities: (i) While CARS signal appears at a new wavelength, the SRS signal is detected at the exact wavelength of pump or Stokes beams; (ii) The CARS beam is highly directional, and can be effectively collected with low numerical aperture (NA) collection optics. In contrast, the SRS beam exactly follows pump and Stokes beams, and therefore, the focusing and

collection optics with similar NA are required for optimal collection of SRS signal; (iii) The epi-detected CARS signal arises from small objects or from reflection of the forward signal, whereas the epi-detected SRS solely relies on the back-scattered photons. Because the SRS signal has the same wavelengths as the excitation beams, polarization separation is used for epi-SRS detection [14, 59]; (iv) In contrast to CARS, the phase matching conditions of SRS are always satisfied, which eliminates the need for tight focusing. Moreover, in the case of Gaussian pump and Stokes beams focused collinearly through a sample, Owyoung and Jones [57] derived in 1977 an analytical expression for the SRS signal intensity, which is independent of focusing conditions and linear to both pump and Stokes powers. In microscopy, this independence of focusing conditions has been demonstrated by Slipchenko *et al.* [59], who imaged large particles in pharmaceutical solid dosage forms using low NA objective. Although the SRS signal is free from the non-resonant background, there are a number of optical processes, including stimulated absorption or emission [18, 69], the optical Kerr effect, cross phase modulation, and the thermal lensing effect [102], which could potentially produce the background. In practice, stimulated absorption or emission [18, 69] can be minimized by using longer excitation wavelengths. The optical Kerr effect and cross phase modulation can be minimized using frequency modulation instead of amplitude modulation [103]. Thermal lensing effect [102] can be minimized by using a high NA objective for signal collection [14, 104] or by high-frequency modulation (> 1 MHz) [105, 106]. Most SRS experiments have been done with crystal-based OPOs, but a recent paper showed the promise of using a fiber laser for SRS imaging [107].

3.7 Implementation of pump-probe and photothermal modalities

The presence of two excitation beams in CARS microscope also opens opportunities for developing pump-probe microscopy. Since the pump-probe technique measures the modulation of the probe beam intensity induced by the interaction of the modulated pump beam with a sample, the implementation of pump-probe modality is similar to SRS and can be realized by phase-sensitive detection [18, 69]. In previous work, photothermal microscopy was done with cw lasers [20]. The pulsed laser on a CARS microscope enabled photothermal imaging based on two-photon absorption [108].

3.8 Coupling CARS and SRS with spontaneous Raman

A drawback of single-frequency CARS and SRS microscopy is that each image only contains information from a single Raman shift. The lack of spectral information can be partially compensated by acquiring Raman spectra at the points of interest in a CARS or SRS image. To realize Raman microspectroscopy on the CARS microscope, the laser source should have sufficient spectral resolution, and therefore ps laser source is optimal. In case of fs laser system, the spectral bandwidth can be reduced by narrowband filter. Slipchenko *et al.* [104] first realized Raman microspectroscopy on a ps laser based CARS microscope by adding a spectrometer to one of the optical ports of the microscope and using appropriate filters to reject the scattering of the excitation laser. To reject background signal and achieve 3-D spatial resolution, the spectrometer slit assembly has been replaced with a pinhole. Due to NIR nature of the Raman signal, the spectrum obtained by charge-coupled device (CCD) might show strong etalon effect. Such effect can be avoided by using front-illuminated or deep-depleted CCD detectors. Coupling of CARS and Raman has been used for spectral analysis of lipids in *C. elegans* [109], drug tablets [59], and cellulose fibers [110].

4. Applications to biological and biomedical science

4.1. Study of white matter

White matter of the central nervous system (CNS) is enriched in myelin sheath, which is a multi-lamellar oligodendroglial cell membranes wrapping around axons [111]. The lamellar

structure of myelin sheath has been characterized by traditional methods including electron microscopy, histology, and immunofluorescence [112]. However, these methods can only examine fixed tissues, and so prevent dynamic studies of cellular activities during the disease process. Clinical imaging tools, such as magnetic resonance imaging (MRI), have been used for in vivo imaging of white matter, but they lack single-cell resolution [75]. By taking advantage of high lipid content in myelin sheath (~70% lipid by weight) [113], Wang *et al*. in 2005, for the first time, reported the application of CARS microscopy to label-free visualization of myelin sheaths under physiological conditions [114]. Owing to submicron resolution of CARS microscopy, detailed structures of the node of Ranvier and Schmidt-Lanterman incisure were resolved [114].

In the past several years, the integration of multiple NLO modalities on the same CARS microscopic platform has enabled CARS imaging of myelin sheath, SFG or SHG imaging of astrocyte processes and microtubules, and TPEF imaging of other important biological components (e.g. calcium activity) with the aid of fluorescence probes, simultaneously [98, 115–118]. The interactions between myelinated axons and other essential components (e.g. astrocyte processes, calcium activity) in the white matter were directly visualized. These capabilities of multimodal NLO microscopy open up new opportunities to investigate the pathological pathways of demyelinating diseases and explore better therapeutic strategies for the diseases.

Demyelination, or the loss of myelin sheath around the axons, impairs action potential conduction along the axons, which in turn accounts for numerous neurological disorders including multiple sclerosis, and spinal cord injury [112, 113]. The molecular mechanisms underlying myelin damage, however, is not well understood. By using multimodal NLO microscopy, Fu *et al*. have carried out mechanistic studies of myelin damage in different demyelination models [115, 116]. By incorporating TPEF imaging of the calcium activity indicator with CARS imaging of myelin sheath, Lysophosphatidyl choline (Lyso-PtdCho) was shown to not only induce myelin swelling but also cause Ca^{2+} influx into the axons [116]. In another study, Fu *et al*. first used CARS imaging to show that glutamate induced paranodal myelin splitting and retraction [115]. TPEF imaging and immunohistochemistry were then used to reveal that glutamate inhibits axonal conduction via breaking axo-glial junctions and exposing juxtaparanodal K^+ channels [115].

As one of the neurological disorders, spinal cord injury (SCI) causes immediate disruption to neuronal membranes and Ca^{2+} influx into axons, followed by subsequent secondary damages [119]. A key therapeutic strategy for SCI is sealing the damaged membranes at an early stage [120, 121]. Recently, Shi *et al*. used multimodal NLO microscopy to evaluate the effectiveness of copolymer micelles in repairing SCI *in vivo* [122]. In this study, CARS imaging was used to monitor the morphological changes of myelin sheath after injury and treatments with different polymers. TPEF imaging was used to map the calcium distribution in myelinated axons [122]. As shown in Fig. 3, intraaxonal free Ca^{2+} level was much higher in compression-injured spinal cord (Fig. 3b) than that in healthy one (Fig. 3a). With low-concentration micelle treatment, injured spinal cord showed significantly reduced Ca^{2+} influx into axons (Fig. 3c).

To summarize, the capability of simultaneous observation of various components and their interactions in the white matter makes multimodal NLO microscopy an attractive tool for the studies of neurological diseases. Future studies focusing on *in vivo* multimodal NLO imaging of the white matter would significantly contribute to the understanding of the dynamics of disease progression.

4.2. Study of lipid metabolism

4.2.1 Lipid droplet biology—Lipid droplets (LDs) are complex proteolipid organelles that often play dynamic roles in various aspects of lipid metabolism [123–125]. The aberrant accumulation of LDs is associated with some of the most widespread human diseases, such as obesity, diabetes type II, and atherosclerosis [123–125]. With the capability of label-free visualization of LDs, CARS microscopy has been used to monitor LDs dynamics in many systems [126–130]. By combining CARS with TPEF imaging, further in-depth studies on LD biology have been conducted. Nan *et al.* revealed the interaction between LDs and mitochondria, which were labeled with fluorescent probe, in adrenal cortical cells [130]. By coupling the immunostaining of LDs-associated proteins, Yamaguchi *et al.* found that Comparative Gene Identification-58 protein facilitated lipolysis of LDs in cooperation with perilipin [128]. With the help of fluorophore-labeled insulin, Le *et al.* unraveled that insulin accounted for the phenotypic variability in LDs accumulation among clonal cells [126]. By utilizing curcumin autofluorescence, Kim *et al.* found that curcumin could inhibit adipocyte differentiation [129]. Through live cell fluorescence imaging of viral RNA and simultaneously CARS imaging of LDs, Lyn *et al.* highlighted the significance of lipid metabolism in viral replication [127]. Given that fluorescent proteins-tagged LDs-associated proteins have been made available [131], simultaneous CARS and TPEF imaging would be able to provide new insights into the dynamic association between lipids and proteins, which are critical for LDs formation and function in living cells.

4.2.2 Lipid metabolism in model organism—Although nematode *C. elegans* is distant from mammals, the pathways of lipid metabolism in human are highly conserved in *C. elegans* [132, 133]. Highly tractable genetics that are critical in lipid metabolism make *C. elegans* an attractive model for the integrative studies of lipid metabolism regulation and related metabolic diseases [134, 135]. The transparent nature of *C. elegans* facilitates the studies of lipid storage by microscopy-based methods [136]. Traditionally, the lipid stores in intestinal and hypodermal cells are visualized by staining with lipophilic dyes including Sudan black and Nile Red. However, the labeling efficiency and accuracy have recently been challenged [136]. Although fixative staining methods provide reproducible data, their results may be interfered with fluorescence signals from the autofluorescent particles in lysosome-related organelles [137, 138]. Feeding worms with vital dyes was thought to monitor dynamics of lipid storage, but the vital dyes have been recently shown to be just sequestrated in autofluorescent particles, rather than label any fat stores in intestine or hypodermis [137, 139]. Moreover, the dynamic changes of lipid composition for individual LDs are not possible to be measured with traditional analytical chemistry methods such as gas chromatography. Therefore, a non-invasive and label-free method to quantitatively analyze lipid storage and composition in living *C. elegans* is critically needed.

Several pilot studies showcase the capability of CARS microscopy for label-free imaging of lipid storage in living *C. elegans*. As the first study, Hellerer *et al.* demonstrated that CARS microscopy not only overcame the limitations of fluorescent staining methods, but also accurately assessed the impact of genetic deficiencies in lipid metabolism (e.g. insulin signaling pathway) on lipid storage, distribution, and packing density [140]. In a follow-up study by Morck *et al.*, CARS imaging did not detect any cholesterol lowering drug-induced reduction of lipid storage as detected by Nile Red staining [141]. More recently, by combining CARS imaging with TPEF imaging, Le *et al.* and Yen *et al.* revealed two distinctive lipid species in *C. elegans*: a neutral lipid species in both intestine and hypodermis and an autofluorescent particle species only found in intestine [109, 137]. Le *et al.* also found that genetic mutations of lipid signaling pathways including peroxidation and desaturation altered the accumulation of neutral lipids and autofluorescent particles (Fig. 4a–b) [109]. Other than *C. elegans*, some other model organisms, such as zebrafish and yeast

Saccharomyces cerevisiae, are also gaining popularity in lipid research, as shown by and Holtta-Vuori *et al.* [142] and Brackmann *et al.* [143] (for review see [144]).

By coupling confocal Raman microspectroscopy with CARS and TPEF imaging, the chemical composition of neutral lipids and antofluorescent particles can be characterized. The intensity ratio between Raman bands at 1660 cm^{-1} and 1445 cm^{-1} has been used as a reliable measure of lipid chain unsaturation [109]. As shown in Fig. 4d, neutral lipid droplets in eggs, whose structure is depicted in Fig. 4c, have higher level of lipid chain unsaturation compared with those in adult intestine. Interestingly, the ester bond around 1742 cm^{-1} is absent in autofluorescent particles, which suggests that these particles do not contain neutral lipids. Moreover, the prominent Raman bands for phenytalanine around 1004 cm^{-1}, for amide III region 1225–1350 cm^{-1}, for amide I around 1660 cm^{-1}, and for CH_3 bonds around 2940 cm^{-1} imply that the autofluorescent particles are rich in proteins rather than lipids. Taking advantage of recent advances in *C. elegans* genetics [134] and microfluidic chamber-based lifelong *C. elegans* imaging [145], it is foreseeable that multimodal NLO microscopy presents an unprecedented opportunity to study dynamic lipid regulation in living *C. elegans*.

4.2.3 Intestinal lipid absorption—Intestinal lipid absorption happens in enterocytes, where free fatty acids (FFAs) and monoacylglycerols are resynthesized into triacylglycerols (TGs) and packaged into the chylomicrons for export into the lymphatic system through exocytosis. [146]. Traditionally, the process of intestinal lipid absorption was visualized by histology and electron microscopy, which hinder the investigation of the dynamic process. CARS microscopy has been first used by Zhu *et al.* to reveal a dynamic, cytoplasmic triacylglycerol pool in enterocytes, which challenges the conventional paradigm [147]. In the follow-up studies by Lee *et al.*, the role of diacylglycerol acyltransferase 1, a key enzyme in TG biosynthesis, in dietary fat absorption was carefully studied [148]. Moreover, TPEF imaging of lipid droplet associated proteins was recently combined with CARS imaging to study the association of the proteins with cytoplasmic LDs in mouse enterocytes during dietary fat absorption [149]. Future applications of multimodal NLO microscopy are expected to contribute new knowledge on the impact of genes and enzymes on intestinal lipid absorption, and the responses of drugs for reduction of energy intake.

4.3. Atherosclerosis research

Atherosclerosis is the major cause of cardiovascular diseases, which have kept the highest mortality rate in the United States for decades [150]. Current imaging methods for the diagnosis of atherosclerosis include x-ray angiography, MRI, intravascular ultrasound (IVUS), computed tomography (CT), and optical coherence tomography (OCT) [151–153]. The capabilities of these methods are limited by either low spatial resolution or a lack of chemical specificity. Thus, there is a need for development of an imaging-based diagnostic tool to evaluate morphological features with subcellular resolution and molecular compositions that are closely associated with plaque vulnerability.

Recently, multimodal NLO microscopy has been applied by Le *et al.* and Wang *et al.* to visualize multiple components of arterial walls and atherosclerotic lesions in a label-free manner, for instance CARS imaging of lipid-rich foam cells, SFG or SHG imaging of collagen type I fibrils, and TPEF imaging of elastin [154, 155]. The plaque vulnerability was shown to be associated with increased accumulation of foam cells and reduced and disorganized collagen type I fibrils [154, 155]. Wang *et al.* in another study demonstrated the capability of multimodal NLO microscopy to accurately identify different stages of atherosclerotic lesions by quantifying lipid and collagen content [156]. These initial works have been followed up by studies of other animal models, such as ApoE-deficient mice and

myocardial infarction-prone rabbits [157, 158]. Most recently, Kim *et al.* used multiplex CARS to correlate the morphology with chemical profile of atherosclerotic lipids [159]. The improved penetration depth is critically needed for clinical application of multimodal NLO microscopy for atherosclerosis diagnosis. The further developments of CARS endoscopy and combinatorial platform with other diagnostic imaging tools, such as OCT and IVUS, would significantly benefit the diagnosis of atherosclerosis.

4.4. Cancer research

4.4.1 Detection of cancer—Despite considerable scientific gains in cancer diagnosis and treatment, cancer remains to threaten human's life [160]. Current clinically-used imaging methods for cancer diagnosis include x-ray, CT, MRI, and OCT [161, 162]. The capabilities of these methods are limited by either low spatial resolution or a lack of chemical specificity, which, in turn, may hamper the identification of the margin of cancer tissue. Thus, there is a need for development of an imaging-based diagnostic tool to evaluate morphological features with subcellular resolution and molecular compositions that are closely associated with tumor malignancy.

The application of CARS microscopy to cancer detection was initiated by Evans *et al*., who observed lower lipid content but higher protein content in brain tumor tissues compared with those in the normal tissues [163]. Because lipid-rich cell membranes and lipid-poor cell nuclei generate substantial contrast in CARS imaging, CARS microscopy actually can be used to visualize tumor cells with submicron resolution in a label-free manner (Fig. 5). Moreover, simultaneous CARS and SFG imaging enables label-free visualization of cell arrangement and collagen type I fibrils organization. Fig. 5a shows the spectrum of CARS, TPEF, and SFG signals obtained simultaneously from different components of the mammary tissue. Because of the lack of normal glandular structures and low cytoplasm/nucleus ratio in mammary tumors [164], morphological depiction by CARS imaging would be able to distinguish tumor tissues from normal tissues. Because of the presence of disorganized and straight collagen type I fibrils in malignant mammary tumors [165, 166], selective collagen I imaging by SFG microscopy would be able to distinguish malignant tumors (Fig. 5c–d) from benign tumors (Fig. 5b). These findings suggest that with the aid of endoscopy [167], multimodal NLO imaging could have the potential to serve as image-guided tool for cancer diagnosis.

4.4.2 Tumor microenvironment—It has been realized that disordered tissue microenvironment could alter phenotypic behavior of tumor cells, and then induce or promote tumor development, progression, and metastasis [168, 169]. multimodal NLO microscopy has been used to image significant components of mammary tumor microenvironment including adipocytes, collagen type I fibrils, blood vessels, and macrophages [170]. Based on this demonstration, Le *et al.* further found that the size of adipocytes in mammary gland and collagen content in mammary tumor microenvironment were increased in obese rats compared with those in lean rats, which suggests the role of obesity in modifying tumor microenvironment [170]. As shown in Fig. 5, SFG imaging specifically recognizes dense wavy collagen fibrils in mammary adenoma, as opposed to the thin straight collagen fibrils in mammary adenocarcinoma. This observation is consistent with several previous studies, which showed that aberrations in type I collagen production and degradation have become one of the hallmarks of tumor microenvironment [165, 166, 171, 172]. Together these studies suggest that multimodal NLO microscopy holds the promise to become a valuable tool for the study of tumor microenvironment in the future.

4.4.3 Lipids in cancer development—Although excess intracellular lipids have been observed in various kinds of cancer [164, 173–176], the mechanism underling the link

between lipid metabolism and cancer development remains largely unknown. Recently, by employing multimodal NLO microscopy, Le *et al*. evaluated cancer cell behaviors in excess lipid environments *in vitro* and *in vivo* [177]. It was shown that excess FFAs not only induced intracellular lipid accumulation in cancer cells, but also perturbed cancer cell membranes [177]. Lipid-rich cancer cells showed more aggressive behaviors including reduced cell-cell contact, increased cell-substrate adhesion, and promoted migration and invasion [177]. In this study, CARS imaging enabled visualization of LDs accumulation and cell membrane perturbation, whereas SFG imaging permitted observation of migrating cancer cells on collagen fibrils. More interestingly, circulating tumor cells (CTCs) also accumulated considerable LDs, which suggests possible development of label-free intravital CARS flow cytometry for clinical CTC detection. Future studies that correlate the amount and composition of intracellular lipids with the aggressiveness of cancer cells would provide better understanding of the roles of lipids in cancer development.

4.5. Study of skin

As the soft outer covering, skin performs various functions including protection, heat regulation, sensation, storage and synthesis [178]. Because many components in the skin are rich in lipids, Evans *et al.* for the first time demonstrated CARS imaging of the lipid-rich structures including corneocytes, sebaceous glands, and subcutaneous adipocytes in the skin of a live mouse [77]. Label-free and high-speed CARS imaging enabled real-time monitoring of time-dependent diffusion of mineral oil in the skin [77]. Freudiger et al. furthered demonstrated SRS imaging of mouse ear skin with high sensitivity and no nonresonant background [14]. More recently, by combining SHG imaging with CARS imaging, Zimmerley *et al.* found that DMSO gradually caused morphological changes to the collagen type I matrix in the skin [179]. By combining confocal Raman microspectroscopy with CARS imaging, Slipchenko *et al.* showed that the lipids accumulated in sebaceous glands had much higher saturation level and lipid packing density compared with those in adipocytes [104]. These studies demonstrate the ability of multimodal NLO microscopy to evaluate the effects of chemical compounds, such as skin care product, on the skin tissue.

4.6. Label-free detection of chromophores

Chromophores, such as hemoglobin and melanin, reside all over the body and play important roles in maintaining cell function [69, 180]. Due to barely discernible fluorescence, it was difficult to image chromophores based on their endogenous contrasts. Recently, there have been three developments of NLO microscopy, which are capable of producing strong contrasts from chromophores without photodamage. One is pump-probe transient absorption microscopy, which was used to image both skin pigmentation and red blood cells [18]. Oxyhemoglobin and deoxyhemoglobin could also be distinguished using this setup [18]. The second one is stimulated emission microscopy, which was used to visualize chromoproteins, non-fluorescent variants of the green fluorescent protein, and microvascular structures based on endogenous contrast of hemoglobin [69]. The third one is two-photon excited photothermal lens microscopy, which was used to detect individual red blood cells [108]. These new developments and applications would stimulate further studies of the roles of various chromophores in human health and diseases.

4.7. Tissue engineering

The study of cell behaviors in a 3D culture model is crucial for tissue engineering research. For real-time monitoring of cell activities in 3D culture, label-free, chemical-selective, and high-speed NLO imaging is desirable. By using CARS imaging, Conovaloff *et al.* monitored the growth of neurites in conditioned hydrogel tissue scaffold over time [181]. By combining CARS with SHG microscopy, Brackmann *et al.* have visualized the formation of

cellulose scaffolds in real time and also the cell integration into the cellulose scaffold [182]. These studies show the promise of CARS imaging to assist in designing better tissue scaffold for organogenesis.

4.8. Study of biomass conversion

Biomass conversion provides alternative ways to produce energy [183]. However, the biomass conversion kinetics has not been well understood yet. Very recently, Saar *et al.* used SRS microscopy to map the distribution of two important chemical species in the biomass conversion process, lignin and cellulose, in corn stover, without labeling [60]. They further showed real-time SRS imaging of a delignification reaction in corn stover (Fig. 6). This study suggests that SRS imaging holds the promise for more thorough studies of biomass conversion process.

4.9. Drug formulation and delivery

In order to enhance the therapeutic effect of a pharmaceutical compound with minimum side effects, efforts have been made to design better drug delivery systems. Sustained and controlled release of drugs is generally desirable [184]. Although high-performance liquid chromatography (HPLC) is widely used to measure drug release profile, the information regarding drug redistribution during release is missing in HPLC measurement. CARS microscopy was first used by Kang *et al.* to monitor paclitaxel redistribution and dissolution in various drug-eluting stent films during the release process [185–187]. Later, CARS microscopy was also used to monitor drug dissolution in tablets [188]. Very recently, Slipchenko *et al.* employed the newly developed compound Raman microscope, capable of SRS imaging and confocal Raman microspectroscopy, to map the spatial distribution of active pharmaceutical ingredient (API) and excipients in tablets from six different manufacturers (Fig. 7) [59]. The capabilities of both high-speed vibrational imaging and spectral analysis make the compound Raman microscope a desirable tool for studies of drug delivery systems.

4.10. NLO imaging of nanomaterials *in vitro* and *in vivo*

Owing to unique optical properties, nanomaterials have been extensively used as probes for live cell and animal imaging [49, 189–192]. The strong intrinsic nonlinearity of these nanomaterials has recently caught substantial attentions [193–195]. In this section, we discuss the application of electronic-resonance-enhanced FWM and transient absorption microscopy to imaging various types of nanomaterials.

4.10.1 Gold nanostructures—Despite the wide use of gold nanostructures as multiphoton luminescent imaging agents [193], the broad fluorescent spectral profile makes gold nanostructures difficult to be distinguished from other fluorescent molecules. In contrast, electronic-resonance-enhanced FWM signals from various gold nanostructures including coupled gold nanoparticles [196], gold NRs [51], and gold NWs [53] have shown narrow spectral profiles at well defined frequencies. In the study of gold NR, Jung *et al.* found that FWM signal was enhanced not only by surface plasmon resonance, but also by aggregation of NRs [51]. In another study by Kim *et al.*, gold zigzag NWs exhibited a strong polarization-dependent FWM signal [53]. Such strong FWM responses from gold nanostructures are intriguing for future applications of these nanostructures in biomedical imaging.

4.10.2 Silicon nanowire (SiNW)—SiNW is a nanomaterial with precisely controllable size, shape, and surface chemistry. Very recently, Jung *et al.* found intrinsically intensive and stable FWM and THG emissions from SiNWs as small as 5 nm with the narrow and

well defined spectral profiles (Fig. 8a–b) [52]. The strong FWM signals from SiNWs permitted real-time monitoring of the circulation of SiNWs in the peripheral blood of a live mouse. The biodistribution of SiNWs in various tissues is shown in Fig. 8c–e [52]. SiNWs is anticipated to be a novel agent for deep tissue and *in vivo* imaging. The interactions between nanomaterials and biological cells or tissues could be addressed by combining electronic-resonance-enhanced FWM microscopy with well-established TPEF, CARS and SFG microscopy.

4.10.3 Carbon nanotube—Owing to intrinsic optical properties, carbon nanotubes have been visualized in biological environment by Raman [197–199] and photoacoustic [200] microscopy. Recently, Kim *et al.* utilized FWM microscopy to examine individual carbon nanotubes [54]. When the excitation was resonant with electronic transitions of the nanotube, SWNTs exhibited large FWM contrast at the anti-Stokes frequency [54]. Jung *et al.* have used transient absorption microscopy to distinguish semiconducting and metallic SWNTs [68]. With the capability of detecting the metallic state in individual SWNTs, transient absorption microscopy holds a great potential for screening of carbon nanotubes in nano-electronics applications.

5. Discussion and Outlook

As shown in this review, by integrating the strengths of each NLO imaging modality, different structures and their interactions in a complex biological system can be simultaneously visualized. The integration of confocal Raman microspectroscopy onto a multimodal NLO microscope further facilitates compositional analysis of the biological structure of interest [104, 109]. Moreover, the capability of high-speed, chemical-selective imaging makes multimodal NLO microscopy an appealing tool to study dynamic processes of disease development *in vivo* [118, 201, 202]. CARS microscopy should allow longitudinal studies of lipid metabolism in the same living model organisms over time, which could provide new understanding of the role of ageing in the regulation of lipid metabolism. Other promising directions include label-free imaging of organogenesis and drug delivery. Notably, the polarization sensitivity of CARS provides additional structural information and has been utilized to study molecular orientations in myelin [114, 203], single lipid bilayer [204], cellulose fiber [110], and crystal of pure fourth-order symmetry [205].

Toward translational research, multimodal NLO microscopy has been shown to be capable of diagnosing diseases in live tissues and even in live animals [75, 156]. This promotes a way to enhance the impact of the technique by moving it from bench to the bedside. In order to achieve this ultimate goal, several technical difficulties need to be overcome. Increasing penetration depth will be one of the challenges. Although miniature microscope objective has been developed to physically enhance the penetration depth [206], new concepts of vibrational imaging that intrinsically allow deep tissue penetration would be highly appreciated. To miniaturize and simplify the system, compact laser sources and optical fiber delivery have been developed [86, 90, 93, 167, 207]. Furthermore, the demonstration of CARS endoscopy [167, 207] took another step towards clinical application. It is expected that an affordable and user-friendly multimodal NLO microscope would become a valuable tool for disease diagnosis in hospital.

Finally, we envision that CARS microscope will continue to serve as a valuable platform for expanding the NLO microscopy family. The CARS microscope can be directly used for TPEF imaging, SHG imaging, Raman microspectroscopy, and has recently been employed for FWM imaging of nanomaterials such as gold NRs, semiconducting NWs and carbon nanotubes. Adding a optical modulate, a photodiode detector and a lock-in amplifier to a

CARS microscope enabled heterodyne detection of a variety of NLO processes such as stimulated Raman scattering and transient absorption. With no doubt, coupling of these modalities offers unprecedented opportunities for study of complex biological systems and individual nanomaterials.

References

1. Zipfel WR, Williams RM, Webb WW. Nonlinear magic: Multiphoton microscopy in the biosciences. Nat Biotechnol. 2003; 21:1369–1377. [PubMed: 14595365]
2. Helmchen F, Denk W. Deep tissue two-photon microscopy. Nat Methods. 2005; 2:932–940. [PubMed: 16299478]
3. Campagnola PJ, Loew LM. Second-harmonic imaging microscopy for visualizing biomolecular arrays in cells, tissues and organisms. Nat Biotechnol. 2003; 21:1356–1360. [PubMed: 14595363]
4. Yelin D, Silberberg Y. Laser scanning third-harmonic-generation microscopy in biology. Opt Express. 1999; 5:169–175. [PubMed: 19399061]
5. Cheng JX. Coherent anti-Stokes Raman scattering microscopy. Appl Spectrosc. 2007; 61:197A–206A. [PubMed: 17910784]
6. Cheng JX, Xie XS. Coherent anti-Stokes Raman scattering microscopy: instrumentation, theory, and applications. J Phys Chem B. 2004; 108:827–840.
7. Le TT, Yue S, Cheng JX. Shedding new light on lipid biology with CARS microscopy. J Lipid Res. 2010
8. Evans CL, Xie XS. Coherent anti-Stokes Raman scattering microscopy: chemically selective imaging for biology and medicine. Annu Rev Anal Chem. 2008; 1:883–909.
9. Volkmer A. Vibrational imaging and microspectroscopies based on coherent anti-Stokes Raman scattering microscopy. J Phys D: Appl Phys. 2005; 38:R59–R81.
10. Wang HW, Fu Y, Le TT, Wang H, Cheng JX. Chasing lipids in health and diseases by coherent anti-Stokes Raman scattering microscopy. Vib Spectrosc. 2009; 50:160–167. [PubMed: 19763281]
11. Wang Y, Lin CY, Nikolaenko A, Raghunathan V, Potma EO. Four-wave mixing microscopy of nanostructures. Adv Opt Photon. 2011; 3:1–52.
12. Ozeki Y, Dake F, Kajiyama Si, Fukui K, Itoh K. Analysis and experimental assessment of the sensitivity of stimulated Raman scattering microscopy. Opt Express. 2009; 17:3651–3658. [PubMed: 19259205]
13. Nandakumar P, Kovalev A, Volkmer A. Vibrational imaging based on stimulated Raman scattering microscopy. New J Phys. 2009; 11:033026.
14. Freudiger CW, Min W, Saar BG, Lu S, Holtom GR, He C, Tsai JC, Kang JX, Xie XS. Label-free biomedical imaging with high sensitivity by stimulated Raman scattering microscopy. Science. 2008; 322:1857–1861. [PubMed: 19095943]
15. Nandakumar, P.; Kovalev, A.; Muschielok, A.; Volkmer, A. Vibrational imaging and microspectroscopies based on coherent anti-Stokes Raman scattering microscopy. the 8th European/French Israeli Symposium on Nonlinear and Quantum Optics, Mo-B. 2005. http://www.weizmann.ac.il/conferences/frisno8/program.html
16. Ploetz E, Laimgruber S, Berner S, Zinth W, Gilch P. Femtosecond stimulated Raman microscopy. Appl Phys B. 2007; 87:389–393.
17. Saar BG, Freudiger CW, Reichman J, Stanley CM, Holtom GR, Xie XS. Video-Rate Molecular Imaging in Vivo with Stimulated Raman Scattering. Science. 2010; 330:1368–1370. [PubMed: 21127249]
18. Ye T, Fu D, Warren WS. Nonlinear Absorption Microscopy. Photochem Photobiol. 2009; 85:631–645. [PubMed: 19170931]
19. Hartland GV. Ultrafast studies of single semiconductor and metal nanostructures through transient absorption microscopy. Chem Sci. 2010; 1:303–309.
20. Gaiduk A, Ruijgrok PV, Yorulmaz M, Orrit M. Detection limits in photothermal microscopy. Chem Sci. 2010; 1:343–350.

21. Cognet L, Berciaud Sp, Lasne D, Lounis B. Photothermal Methods for Single Nonluminescent Nano-Objects. Anal Chem. 2008; 80:2288–2294. [PubMed: 18456908]
22. Debarre D, Supatto W, Pena AM, Fabre A, Tordjmann T, Combettes L, Schanne-Klein MC, Beaurepaire E. Imaging lipid bodies in cells and tissues using third-harmonic generation microscopy. Nat Methods. 2006; 3:47–53. [PubMed: 16369553]
23. Olivier N, Luengo-Oroz MA, Duloquin L, Faure E, Savy T, Veilleux I, Solinas X, Debarre D, Bourgine P, Santos A, Peyrieras N, Beaurepaire E. Cell Lineage Reconstruction of Early Zebrafish Embryos Using Label-Free Nonlinear Microscopy. Science. 2010; 329:967–971. [PubMed: 20724640]
24. Supatto W, Debarre D, Moulia B, Brouzes E, Martin JL, Farge E, Beaurepaire E, Anderson KV. In vivo Modulation of Morphogenetic Movements in Drosophila Embryos with Femtosecond Laser Pulses. Proc Natl Acad Sci USA. 2005; 102:1047–1052. [PubMed: 15657140]
25. Zipfel WR, Williams RM, Christie R, Nikitin AY, Hyman BT, Webb WW. Live Tissue Intrinsic Emission Microscopy Using Multiphoton-Excited Native Fluorescence and Second Harmonic Generation. Proc Natl Acad Sci USA. 2003; 100:7075–7080. [PubMed: 12756303]
26. Zoumi A, Yeh A, Tromberg BJ. Imaging Cells and Extracellular Matrix in vivo by Using Second-Harmonic Generation and Two-Photon Excited Fluorescence. Proc Natl Acad Sci USA. 2002; 99:11014–11019. [PubMed: 12177437]
27. Duncan MD, Reintjes J, Manuccia TJ. Scanning coherent anti-Stokes Raman microscope. Opt Lett. 1982; 7:350–352. [PubMed: 19714017]
28. Denk W, Strickler JH, Webb WW. Two-photon laser scanning fluorescence microscopy. Science. 1990; 248:73–76. [PubMed: 2321027]
29. Barad Y, Eisenberg H, Horowitz M, Silberberg Y. Nonlinear scanning laser microscopy by third harmonic generation. Appl Phys Lett. 1997; 70:922–924.
30. Squier J, Muller M, Brakenhoff G, Wilson KR. Third harmonic generation microscopy. Opt Express. 1998; 3:315–324. [PubMed: 19384376]
31. Masters, BR.; So, PTC. Handbook of Biomedical Nonlinear Optical Microscopy. Oxford University Press; Oxford, New York: 2008.
32. Boyd, RW. Nonlinear Optics. Academic; New York: 2003.
33. Cheng JX, Volkmer A, Book LD, Xie XS. An epi-detected coherent anti-Stokes Raman scattering (E-CARS) microscope with high spectral resolution and high sensitivity. J Phys Chem B. 2001; 105:1277–1280.
34. de Grauw CJ, Vroom JM, van der Voort HTM, Gerritsen HC. Imaging Properties in Two-Photon Excitation Microscopy and Effects of Refractive-Index Mismatch in Thick Specimens. Appl Opt. 1999; 38:5995–6003. [PubMed: 18324119]
35. Ji N, Zhang K, Yang H, Shen YR. Three-Dimensional Chiral Imaging by Sum-Frequency Generation. J Am Chem Soc. 2006; 128:3482–3483. [PubMed: 16536497]
36. Sun CK, Chu SW, Chen SY, Tsai TH, Liu TM, Lin CY, Tsai HJ. Higher harmonic generation microscopy for developmental biology. J Struct Biol. 2004; 147:19–30. [PubMed: 15109602]
37. Wampler RD, Kissick DJ, Dehen CJ, Gualtieri EJ, Grey JL, Wang HF, Thompson DH, Cheng JX, Simpson GJ. Selective Detection of Protein Crystals by Second Harmonic Microscopy. J Am Chem Soc. 2008; 130:14076–14077. [PubMed: 18831587]
38. Kuo TR, Wu CL, Hsu CT, Lo W, Chiang SJ, Lin SJ, Dong CY, Chen CC. Chemical enhancer induced changes in the mechanisms of transdermal delivery of zinc oxide nanoparticles. Biomaterials. 2009; 30:3002–3008. [PubMed: 19232716]
39. Pantazis P, Maloney J, Wu D, Fraser SE. Second harmonic generating (SHG) nanoprobes for in vivo imaging. Proc Natl Acad Sci USA. 2010; 107:14535–14540. [PubMed: 20668245]
40. Cheng JX, Xie XS. Green's function formulation for third-harmonic generation microscopy. J Opt Soc Am B. 2002; 19:1604–1610.
41. Tsang TYF. Optical third-harmonic generation at interfaces. Phys Rev A. 1995; 52:4116. [PubMed: 9912728]
42. Lee WJ, Lee CF, Chen SY, Chen YS, Sun CK. Virtual biopsy of rat tympanic membrane using higher harmonic generation microscopy. J Biomed Opt. 2010; 15:046012. [PubMed: 20799814]

43. Rietdorf, J.; Sun, C-K. Microscopy Techniques. Vol. 95. Springer; Berlin/Heidelberg: 2005. p. 17-56.
44. Yelin D, Oron D, Thiberge S, Moses E, Silberberg Y. Multiphoton plasmon-resonance microscopy. Opt Express. 2003; 11:1385–1391. [PubMed: 19466009]
45. Mooradian A. Photoluminescence of Metals. Phys Rev Lett. 1969; 22:185.
46. Chen CK, de Castro ARB, Shen YR. Surface-Enhanced Second-Harmonic Generation. Phys Rev Lett. 1981; 46:145.
47. Boyd GT, Yu ZH, Shen YR. Photoinduced luminescence from the noble metals and its enhancement on roughened surfaces. Phys Rev B. 1986; 33:7923.
48. Farrer RA, Butterfield FL, Chen VW, Fourkas JT. Highly efficient multiphoton-absorption-induced luminescence from gold nanoparticles. Nano Lett. 2005; 5:1139–1142. [PubMed: 15943457]
49. Wang HF, Huff TB, Zweifel DA, He W, Low PS, Wei A, Cheng JX. In vitro and in vivo two-photon luminescence imaging of single gold nanorods. Proc Natl Acad Sci USA. 2005; 102:15752–15756. [PubMed: 16239346]
50. Park J, Estrada A, Sharp K, Sang K, Schwartz JA, Smith DK, Coleman C, Payne JD, Korgel BA, Dunn AK, Tunnell JW. Two-photon-induced photoluminescence imaging of tumors using near-infrared excited gold nanoshells. Opt Express. 2008; 16:1590–1599. [PubMed: 18542237]
51. Jung Y, Chen H, Tong L, Cheng JX. Imaging Gold Nanorods by Plasmon-Resonance-Enhanced Four Wave Mixing. J Phys Chem C. 2009; 113:2657–2663.
52. Jung Y, Tong L, Tanaudommongkon A, Cheng JX, Yang C. In Vitro and In Vivo Nonlinear Optical Imaging of Silicon Nanowires. Nano Lett. 2009; 9:2440–2444. [PubMed: 19507891]
53. Kim H, Taggart DK, Xiang CX, Penner RM, Potma EO. Spatial control of coherent anti-stokes emission with height-modulated gold zig-zag nanowires. Nano Lett. 2008; 8:2373–2377. [PubMed: 18662040]
54. Kim H, Sheps T, Collins PG, Potma EO. Nonlinear Optical Imaging of Individual Carbon Nanotubes with Four-Wave-Mixing Microscopy. Nano Lett. 2009; 9:2991–2995. [PubMed: 19637886]
55. Woodbury EJ, Ng WK. Ruby Laser Operation in Near IR. Proc Inst Radio Eng. 1962; 50:2367.
56. Jones WJ, Stoicheff BP. Inverse Raman Spectra: Induced Absorption at Optical Frequencies. Phys Rev Lett. 1964; 13:657.
57. Owyoung A, Jones ED. Stimulated Raman spectroscopy using low-power cw lasers. Opt Lett. 1977; 1:152–154. [PubMed: 19680362]
58. Wang H, Fu Y, Cheng JX. Experimental observation and theoretical analysis of Raman resonance-enhanced photodamage in coherent anti-Stokes Raman scattering microscopy. J Opt Soc Am B. 2007; 24:544–552.
59. Slipchenko MN, Chen H, Ely DR, Jung Y, Carvajal MT, Cheng JX. Vibrational imaging of tablets by epi-detected stimulated Raman scattering microscopy. Analyst. 2010; 135:2613–2619. [PubMed: 20625604]
60. Saar BG, Zeng YN, Freudiger CW, Liu YS, Himmel ME, Xie XS, Ding SY. Label-Free, Real-Time Monitoring of Biomass Processing with Stimulated Raman Scattering Microscopy. Angew Chem Int Ed. 2010; 49:5476–5479.
61. Fu D, Ye T, Matthews TE, Chen BJ, Yurtserver G, Warren WS. High-resolution in vivo imaging of blood vessels without labeling. Opt Lett. 2007; 32:2641–2643. [PubMed: 17873920]
62. Fu D, Matthews TE, Ye T, Piletic IR, Warren WS. Label-free in vivo optical imaging of microvasculature and oxygenation level. J Biomed Opt. 2008; 13
63. Fu D, Ye T, Matthews TE, Grichnik J, Hong L, Simon JD, Warren WS. Probing skin pigmentation changes with transient absorption imaging of eumelanin and pheomelanin. J Biomed Opt. 2008; 13
64. Ye T, Yurtsever G, Fischer M, Simon JD, Warren WS. Imaging melanin by two-photon absorption microscopy. Proc SPIE. 2006; 6089:60891X/60891–60891X/60897.
65. Ye T, Pawlak A, Sarna T, Simon JD. Different molecular constituents in pheomelanin are responsible for emission, transient absorption and oxygen photoconsumption. Photochem Photobiol. 2008; 84:437–443. [PubMed: 18248504]

66. Muskens OL, Del Fatti N, Vallee F. Femtosecond Response of a Single Metal Nanoparticle. Nano Lett. 2006; 6:552–556. [PubMed: 16522061]

67. van Dijk MA, Lippitz M, Orrit M. Detection of acoustic oscillations of single gold nanospheres by time-resolved interferometry. Phys Rev Lett. 2005; 95:267406. [PubMed: 16486406]

68. Jung Y, Slipchenko MN, Liu CH, Zhong Z, Yang C, Cheng JX. Fast detection of the metallic state of individual single-walled carbon nanotubes using a transient-absorption optical microscope. Phys Rev Lett. 2010; 105:217401. [PubMed: 21231351]

69. Min W, Lu SJ, Chong SS, Roy R, Holtom GR, Xie XS. Imaging chromophores with undetectable fluorescence by stimulated emission microscopy. Nature. 2009; 461:1105–1109. [PubMed: 19847261]

70. Harada M, Iwamoto K, Kitamori T, Sawada T. Photothermal Microscopy with Excitation and Probe Beams Coaxial Under the Microscope and its Application to Microparticle Analysis. Anal Chem. 1993; 65:2938–2940.

71. Boyer D, Tamarat P, Maali A, Lounis B, Orrit M. Photothermal imaging of nanometer-sized metal particles among scatterers. Science. 2002; 297:1160–1163. [PubMed: 12183624]

72. Zumbusch A, Holtom GR, Xie XS. Three-Dimensional Vibrational Imaging by Coherent Anti-Stokes Raman Scattering. Phys Rev Lett. 1999; 82:4142.

73. Pegoraro AF, Slepkov AD, Ridsdale A, Pezacki JP, Stolow A. Single laser source for multimodal coherent anti-Stokes Raman scattering microscopy. Appl Opt. 2010; 49:F10–F17. [PubMed: 20820199]

74. Müller M, Zumbusch A. Coherent anti-Stokes Raman scattering microscopy. ChemPhysChem. 2007; 8:2156–2170. [PubMed: 17768730]

75. Fu Y, Talavage TM, Cheng JX. New imaging techniques in the diagnosis of multiple sclerosis. Expert Opin Med Diagn. 2008; 2:1055–1065. [PubMed: 19337386]

76. Cheng JX, Jia YK, Zheng GF, Xie XS. Laser-scanning coherent anti-stokes Raman scattering microscopy and applications to cell biology. Biophys J. 2002; 83:502–509. [PubMed: 12080137]

77. Evans CL, Potma EO, Mehron Ph, Cote D, Lin CP, Xie XS. Chemical Imaging of Tissue in Vivo with Video-Rate Coherent Anti-Stokes Raman Scattering Microscopy. Proc Natl Acad Sci USA. 2005; 102:16807–16812. [PubMed: 16263923]

78. Chen H, Wang H, Slipchenko MN, Jung Y, Shi Y, Zhu J, Buhman KK, Cheng JX. A multimodal platform for nonlinear optical microscopy and microspectroscopy. Opt Express. 2009; 17:1282–1290. [PubMed: 19188956]

79. Rocha-Mendoza I, Langbein W, Borri P. Coherent anti-Stokes Raman microspectroscopy using spectral focusing with glass dispersion. Appl Phys Lett. 2008; 93:201103–201103.

80. Hellerer T, Enejder AMK, Zumbusch A. Spectral focusing: High spectral resolution spectroscopy with broad-bandwidth laser pulses. Appl Phys Lett. 2004; 85:25–27.

81. Lu F, Zheng W, Lin J, Huang Z. Integrated coherent anti-Stokes Raman scattering and multiphoton microscopy for biomolecular imaging using spectral filtering of a femtosecond laser. Appl Phys Lett. 2010; 96:133701.

82. Svedberg F, Brackmann C, Hellerer T, Enejder A. Nonlinear microscopy with fiber laser continuum excitation. J Biomed Opt. 2010; 15:026026. [PubMed: 20459271]

83. Potma EO, Jones DJ, Cheng JX, Xie XS, Ye J. High-sensitivity coherent anti-Stokes Raman scattering microscopy with two tightly synchronized picosecond lasers. Opt Lett. 2002; 27:1168–1170. [PubMed: 18026396]

84. Ganikhanov F, Carrasco S, Xie XS, Katz M, Seitz W, Kopf D. Broadly tunable dual-wavelength light source for coherent anti-Stokes Raman scattering microscopy. Opt Lett. 2006; 31:1292–1294. [PubMed: 16642089]

85. Jurna M, Korterik JP, Offerhaus HL, Otto C. Noncritical phase-matched lithium triborate optical parametric oscillator for high resolution coherent anti-Stokes Raman scattering spectroscopy and microscopy. Appl Phys Lett. 2006; 89

86. Kieu K, Saar BG, Holtom GR, Xie XS, Wise FW. High-power picosecond fiber source for coherent Raman microscopy. Opt Lett. 2009; 34:2051–2053. [PubMed: 19571996]

87. Andresen ER, Paulsen HN, Birkedal V, Thogersen J, Keiding SR. Broadband multiplex coherent anti-Stokes Raman scattering microscopy employing photonic-crystal fibers. J Opt Soc Am B. 2005; 22:1934–1938.
88. Kano H, Hamaguchi H. Ultrabroadband (> 2500 cm(−1)) multiplex coherent anti-Stokes Raman scattering microspectroscopy using a supercontinuum generated from a photonic crystal fiber. Appl Phys Lett. 2005; 86
89. Andresen ER, Nielsen CK, Thøgersen J, Keiding SR. Fiber laser-based light source for coherent anti-Stokes Raman scattering microspectroscopy. Opt Express. 2007; 15:4848–4856. [PubMed: 19532731]
90. Pegoraro AF, Ridsdale A, Moffatt DJ, Pezacki JP, Thomas BK, Fu LB, Dong L, Fermann ME, Stolow A. All-fiber CARS microscopy of live cells. Opt Express. 2009; 17:20700–20706. [PubMed: 19997300]
91. Tada K, Karasawa N. Broadband coherent anti-Stokes Raman scattering spectroscopy using soliton pulse trains from a photonic crystal fiber. Opt Comm. 2009; 282:3948–3952.
92. Kee TW, Cicerone MT. Simple approach to one-laser, broadband coherent anti-Stokes Raman scattering microscopy. Opt Lett. 2004; 29:2701–2703. [PubMed: 15605477]
93. Krauss G, Hanke T, Sell A, Trautlein D, Leitenstorfer A, Selm R, Winterhalder M, Zumbusch A. Compact coherent anti-Stokes Raman scattering microscope based on a picosecond two-color Er:fiber laser system. Opt Lett. 2009; 34:2847–2849. [PubMed: 19756125]
94. Cheng JX, Volkmer A, Xie XS. Theoretical and experimental characterization of coherent anti-Stokes Raman scattering microscopy. J Opt Soc Am B. 2002; 19:1363–1375.
95. Volkmer A, Cheng JX, Xie XS. Vibrational imaging with high sensitivity via epidetected coherent anti-Stokes Raman scattering microscopy. Phys Rev Lett. 2001; 87
96. Moreaux L, Sandre O, Charpak S, Blanchard-Desce M, Mertz J. Coherent scattering in multi-harmonic light microscopy. Biophys J. 2001; 80:1568–1574. [PubMed: 11222317]
97. Williams RM, Zipfel WR, Webb WW. Interpreting Second-Harmonic Generation Images of Collagen I Fibrils. Biophys J. 2005; 88:1377–1386. [PubMed: 15533922]
98. Huff TB, Shi Y, Fu Y, Wang H, Cheng JX. Multimodal nonlinear optical microscopy and applications to central nervous system imaging. IEEE Quantum Electron. 2008; 14:4–9.
99. Tong L, Cobley C, Chen J, Xia Y, Cheng JX. Bright Three-Photon Luminescence from Gold/Silver Alloyed Nanostructures for Bioimaging with Negligible Photothermal Toxicity. Angew Chem Int Ed. 2010; 49:3485–3488.
100. Park, Sungnam; Pelton, Matthew; Mingzhao, LIU.; Guyot, S.; Philippe, Scherer; Norbert, F. Ultrafast resonant dynamics of surface plasmons in gold nanorods. Vol. 111. American Chemical Society; Columbus, OH, ETATS-UNIS: 2007.
101. Min W, Lu S, Rueckel M, Holtom GR, Xie XS. Near-Degenerate Four-Wave-Mixing Microscopy. Nano Lett. 2009; 9:2423–2426. [PubMed: 19432483]
102. Uchiyama K, Hibara A, Kimura H, Sawada T, Kitamori T. Thermal lens microscope. Jpn J Appl Phys 1. 2000; 39:5316–5322.
103. Saar BG, Holtom GR, Freudiger CW, Ackermann C, Hill W, Xie XS. Intracavity wavelength modulation of an optical parametric oscillator for coherent Raman microscopy. Opt Express. 2009; 17:12532–12539. [PubMed: 19654655]
104. Slipchenko MN, Le TT, Chen H, Cheng JX. High-speed vibrational imaging and spectral analysis of lipid bodies by compound Raman microscopy. J Phys Chem B. 2009; 113:7681–7686. [PubMed: 19422201]
105. Berciaud S, Cognet L, Blab GA, Lounis B. Photothermal Heterodyne Imaging of Individual Nonfluorescent Nanoclusters and Nanocrystals. Phys Rev Lett. 2004; 93:257402. [PubMed: 15697940]
106. Hiki S, Mawatari K, Hibara A, Tokeshi M, Kitamori T. UV Excitation Thermal Lens Microscope for Sensitive and Nonlabeled Detection of Nonfluorescent Molecules. Anal Chem. 2006; 78:2859–2863. [PubMed: 16615803]
107. Gambetta A, Kumar V, Grancini G, Polli D, Ramponi R, Cerullo G, Marangoni M. Fiber-format stimulated-Raman-scattering microscopy from a single laser oscillator. Opt Lett. 2010; 35:226–228. [PubMed: 20081976]

108. Sijia L, Wei M, Shasha C, Gary RH, Xie XS. Label-free imaging of heme proteins with two-photon excited photothermal lens microscopy. Appl Phys Lett. 2010; 96:113701.
109. Le TT, Duren HM, Slipchenko MN, Hu CD, Cheng JX. Label-free quantitative analysis of lipid metabolism in living Caenorhabditis elegans. J Lipid Res. 2010; 51:672–677. [PubMed: 19776402]
110. Zimmerley M, Younger R, Valenton T, Oertel DC, Ward JL, Potma EO. Molecular orientation in dry and hydrated cellulose fibers: a coherent anti-Stokes Raman scattering microscopy study. J Phys Chem B. 2010; 114:10200–10208. [PubMed: 20684644]
111. Hirano, A.; Liena, JF. The Axon Structure, Function and Pathophysiology. Waxman, SG.; Kocsis, JD.; Stys, PK., editors. Oxford University Press; New York: 1995. p. 49-67.
112. Ludwin, SK. The axon Structure, Function and Pathophysiology. Waxman, SG.; Kocsis, JD.; Stys, PK., editors. Oxford University Press; New York: 1995.
113. Lazzarini, RA. Myelin Biology and its Disorders. Elsevier Academic Press; San Diego, CA: 2004.
114. Wang HF, Fu Y, Zickmund P, Shi RY, Cheng JX. Coherent anti-stokes Raman scattering imaging of axonal myelin in live spinal tissues. Biophys J. 2005; 89:581–591. [PubMed: 15834003]
115. Fu Y, Sun W, Shi Y, Shi R, Cheng JX. Glutamate excitotoxicity inflicts paranodal myelin splitting and retraction. PLoS One. 2009; 4:e6705. [PubMed: 19693274]
116. Fu Y, Wang HF, Huff TB, Shi R, Cheng JX. Coherent anti-stokes Raman scattering imaging of myelin degradation reveals a calcium-dependent pathway in lyso-PtdCho-induced demyelination. J Neurosci Res. 2007; 85:2870–2881. [PubMed: 17551984]
117. Fu Y, Wang HF, Shi RY, Cheng JX. Second harmonic and sum frequency generation imaging of fibrous astroglial filaments in ex vivo spinal tissues. Biophys J. 2007; 92:3251–3259. [PubMed: 17293404]
118. Huff TB, Cheng JX. In vivo coherent anti-Stokes Raman scattering imaging of sciatic nerve tissue. J Microsc. 2007; 225:175–182. [PubMed: 17359252]
119. Young W. Role of calcium in central-nervous-system injuries. J Neurotrauma. 1992; 9:S9–S25. [PubMed: 1588635]
120. Thuret S, Moon LDF, Gage FH. Therapeutic interventions after spinal cord injury. Nat Rev Neurosci. 2006; 7:628–643. [PubMed: 16858391]
121. Bradbury EJ, McMahon SB. Opinion - Spinal cord repair strategies: why do they work? Nat Rev Neurosci. 2006; 7:644–653. [PubMed: 16858392]
122. Shi Y, Kim S, Huff TB, Borgens RB, Park K, Shi R, Cheng JX. Effective repair of traumatically injured spinal cord by nanoscale block copolymer micelles. Nat Nanotechnol. 2010; 5:80–87. [PubMed: 19898498]
123. Fujimoto T, Ohsaki Y, Cheng J, Suzuki M, Shinohara Y. Lipid droplets: a classic organelle with new outfits. Histochem Cell Biol. 2008; 130:263–279. [PubMed: 18546013]
124. Murphy DJ. The biogenesis and functions of lipid bodies in animals, plants and microorganisms. Prog Lipid Res. 2001; 40:325–438. [PubMed: 11470496]
125. Beller M, Thiel K, Thul PJ, Jackle H. Lipid droplets: A dynamic organelle moves into focus. FEBS Lett. 2010; 584:2176–2182. [PubMed: 20303960]
126. Le TT, Cheng JX. Single-cell profiling reveals the origin of phenotypic variability in adipogenesis. PLoS One. 2009; 4:e5189. [PubMed: 19357775]
127. Lyn RK, Kennedy DC, Sagan SM, Blais DR, Rouleau Y, Pegoraro AF, Xie XS, Stolow A, Pezacki JP. Direct imaging of the disruption of hepatitis C virus replication complexes by inhibitors of lipid metabolism. Virology. 2009; 394:130–142. [PubMed: 19747705]
128. Yamaguchi T, Omatsu N, Morimoto E, Nakashima H, Ueno K, Tanaka T, Satouchi K, Hirose F, Osumi T. CGI-58 facilitates lipolysis on lipid droplets but is not involved in the vesiculation of lipid droplets caused by hormonal stimulation. J Lipid Res. 2007; 48:1078–1089. [PubMed: 17308334]
129. Kim CY, Le TT, Chen C, Cheng J-X, Kim Kee-Hong. Curcumin inhibits adipocyte differentiation through modulation of mitotic clonal expansion. J Nutr Biochem. 2010 in press.

130. Nan X, Potma EO, Xie XS. Nonperturbative chemical imaging of organelle transport in living cells with coherent anti-Stokes Raman scattering microscopy. Biophys J. 2006; 91:728–735. [PubMed: 16632501]
131. Miura S, Gan JW, Brzostowski J, Parisi MJ, Schultz CJ, Londos C, Oliver B, Kimmel AR. Functional conservation for lipid storage droplet association among Perilipin, ADRP, and TIP47 (PAT)-related proteins in mammals, Drosophila, and Dictyostelium. J Biol Chem. 2002; 277:32253–32257. [PubMed: 12077142]
132. Mullaney BC, Ashrafi K. C-elegans fat storage and metabolic regulation. Biochim Biophys Acta. 2009; 1791:474–478. [PubMed: 19168149]
133. Ashrafi, K. WormBook. The C elegans Research Community. WormBook; 2007.
134. Ashrafi K, Chang FY, Watts JL, Fraser AG, Kamath RS, Ahringer J, Ruvkun G. Genome-wide RNAi analysis of Caenorhabditis elegans fat regulatory genes. Nature. 2003; 421:268–272. [PubMed: 12529643]
135. Watts JL, Browse J. Genetic dissection of polyunsaturated fatty acid synthesis in Caenorhabditis elegans. Proc Natl Acad Sci USA. 2002; 99:5854–5859. [PubMed: 11972048]
136. Elle IC, Olsen LCB, Pultz D, Rodkaer SV, Faergeman NJ. Something worth dyeing for: Molecular tools for the dissection of lipid metabolism in Caenorhabditis elegans. FEBS Lett. 2010; 584:2183–2193. [PubMed: 20371247]
137. Yen K, Le TT, Bansal A, Narasimhan SD, Cheng J-X, Tissenbaum H. A Comparative Study of Fat Storage Quantitation in Nematode Caenorhabditis elegans Using Label and Label-Free Methods. PLoS One. 2010
138. Clokey GV, Jacobson LA. The autofluorescent “lipofuscin granules” in the intestinal cells of Caenorhabditis elegans are secondary lysosomes. Mech Ageing Dev. 1986; 35:79–94. [PubMed: 3736133]
139. O’Rourke EJ, Soukas AA, Carr CE, Ruvkun G. C. elegans major fats are stored in vesicles distinct from lysosome-related organelles. Cell Metab. 2009; 10:430–435. [PubMed: 19883620]
140. Hellerer T, Axang C, Brackmann C, Hillertz P, Pilon M, Enejder A. Monitoring of lipid storage in Caenorhabditis elegans using coherent anti-Stokes Raman scattering (CARS) microscopy. Proc Natl Acad Sci USA. 2007; 104:14658–14663. [PubMed: 17804796]
141. Morck C, Olsen L, Kurth C, Persson A, Storm NJ, Svensson E, Jansson JO, Hellqvist M, Enejder A, Faergeman NJ, Pilon M. Statins inhibit protein lipidation and induce the unfolded protein response in the non-sterol producing nematode Caenorhabditis elegans. Proc Natl Acad Sci USA. 2009; 106:18285–18290. [PubMed: 19826081]
142. Holtta-Vuori M, Salo VTV, Nyberg L, Brackmann C, Enejder A, Panula P, Ikonen E. Zebrafish: gaining popularity in lipid research. Biochem J. 2010; 429:235–242. [PubMed: 20578994]
143. Brackmann C, Norbeck J, Akeson M, Bosch D, Larsson C, Gustafsson L, Enejder A. CARS microscopy of lipid stores in yeast: the impact of nutritional state and genetic background. J Raman Spectrosc. 2009; 40:748–756.
144. Enejder A, Brackmann C, Svedberg F. Coherent Anti-Stokes Raman Scattering Microscopy of Cellular Lipid Storage. IEEE Quantum Electron. 2010; 16:506–515.
145. Hulme SE, Shevkoplyas SS, McGuigan AP, Apfeld J, Fontana W, Whitesides GM. Lifespan-on-a-chip: microfluidic chambers for performing lifelong observation of C. elegans. Lab Chip. 2010; 10:589–597. [PubMed: 20162234]
146. Phan CT, Tso P. Intestinal lipid absorption and transport. Front Bioscience. 2001; 6:D299–D319.
147. Zhu J, Lee B, Buhman KK, Cheng JX. A dynamic, cytoplasmic triacylglycerol pool in enterocytes revealed by ex vivo and in vivo coherent anti-Stokes Raman scattering imaging. J Lipid Res. 2009; 50:1080–1089. [PubMed: 19218555]
148. Lee B, Fast AM, Zhu J, Cheng JX, Buhman KK. Intestine specific expression of acyl CoA:diacylgylcerol acyltransferase 1 (DGAT1) reverses resistance to diet-induced hepatic steatosis and obesity in Dgat1−/− mice. J Lipid Res. 2010 In press.
149. Lee B, Zhu JB, Wolins NE, Cheng JX, Buhman KK. Differential association of adipophilin and TIP47 proteins with cytoplasmic lipid droplets in mouse enterocytes during dietary fat absorption. Biochim Biophys Acta. 2009; 1791:1173–1180. [PubMed: 19698802]
150. AHA. Heart Disease and Stroke Statistics - 2009 update. 2009

151. Sanz J, Fayad ZA. Imaging of atherosclerotic cardiovascular disease. Nature. 2008; 451:953–957. [PubMed: 18288186]
152. Amirbekian V, Lipinski MJ, Briley-Saebo KC, Amirbekian S, Aguinaldo JGS, Weinreb DB, Vucic E, Frias JC, Hyafil F, Mani V, Fisher EA, Fayad ZA. Detecting and assessing macrophages in vivo to evaluate atherosclerosis noninvasively using molecular MRI. Proc Natl Acad Sci USA. 2007; 104:961–966. [PubMed: 17215360]
153. Nair A, Kuban BD, Obuchowski N, Vince DG. Assessing spectral algorithms to predict atherosclerotic plaque composition with normalized and raw intravascular ultrasound data. Ultrasound Med Biol. 2001; 27:1319–1331. [PubMed: 11731045]
154. Le TT, Langohr IM, Locker MJ, Sturek M, Cheng JX. Label-free molecular imaging of atherosclerotic lesions using multimodal nonlinear optical microscopy. J Biomed Opt. 2007; 12:054007. [PubMed: 17994895]
155. Wang HW, Le TT, Cheng JX. Label-free imaging of arterial cells and extracellular matrix using a multimodal CARS microscope. Opt Commun. 2008; 281:1813–1822. [PubMed: 19343073]
156. Wang HW, Langohr IM, Sturek M, Cheng JX. Imaging and quantitative analysis of atherosclerotic lesions by CARS-based multimodal nonlinear optical microscopy. Arterioscler Thromb Vasc Biol. 2009; 29:1342–1348. [PubMed: 19520975]
157. Lim RS, Kratzer A, Barry NP, Miyazaki-Anzai S, Miyazaki M, Mantulin WW, Levi M, Potma EO, Tromberg BJ. Multimodal CARS microscopy determination of the impact of diet on macrophage infiltration and lipid accumulation on plaque formation in ApoE-deficient mice. J Lipid Res. 2010 In press.
158. Ko, Alex CT.; Ridsdale, Andrew; Smith, Michael SD.; Mostaço-Guidolin, Leila B.; Hewko, Mark D.; Pegoraro, Adrian F.; Kohlenberg, Elicia K.; Schattka, Bernie; Shiomi, Masashi; Stolow, Albert; Sowa, MG. Multimodal nonlinear optical imaging of atherosclerotic plaque development in myocardial infarction-prone rabbits. J Biomed Opt. 2010; 15:020501. [PubMed: 20459215]
159. Kim SH, Lee ES, Lee JY, Lee ES, Lee BS, Park JE, Moon DW. Multiplex Coherent Anti-Stokes Raman Spectroscopy Images Intact Atheromatous Lesions and Concomitantly Identifies Distinct Chemical Profiles of Atherosclerotic Lipids. Circ Res. 2010; 106:1332–1341. [PubMed: 20299664]
160. American Cancer Society. Cancer Facts & Figures 2009. Atlanta: American Cancer Society; 2009.
161. Tsuboi M, Ueda T, Ushizawa K, Ezaki Y, Overman SA, Thomas GJ. Raman tensors for the tryptophan side chain in proteins determined by polarized Raman microspectroscopy of oriented N-acetyl-L-tryptophan crystals. J Mol Struct. 1996; 379:43–50.
162. Tearney GJ, Brezinski ME, Bouma BE, Boppart SA, Pitris C, Southern JF, Fujimoto JG. In vivo endoscopic optical biopsy with optical coherence tomography. Science. 1997; 276:2037–2039. [PubMed: 9197265]
163. Evans CL, Xu XY, Kesari S, Xie XS, Wong STC, Young GS. Chemically-selective imaging of brain structures with CARS microscopy. Opt Express. 2007; 15:12076–12087. [PubMed: 19547572]
164. Rosen, PP. Rosen's Breast Pathology. Lippincott Williams & Wilkins; New York: 2008. p. 555-556.
165. Provenzano PP, Eliceiri KW, Campbell JM, Inman DR, White JG, Keely PJ. Collagen reorganization at the tumor-stromal interface facilitates local invasion. BMC Med. 2006; 4
166. Provenzano PP, Inman DR, Eliceiri KW, Knittel JG, Yan L, Rueden CT, White JG, Keely PJ. Collagen density promotes mammary tumor initiation and progression. BMC Med. 2008; 6
167. Legare F, Evans CL, Ganikhanov F, Xie XS. Towards CARS endoscopy. Opt Express. 2006; 14:4427–4432. [PubMed: 19516594]
168. Tlsty TD, Coussens LM. Tumor stroma and regulation of cancer development. Annu Rev Pathol. 2006; 1:119–150. [PubMed: 18039110]
169. Wiseman BS, Werb Z. Stromal effects on mammary gland development and breast cancer. Science. 2002; 296:1046–1049. [PubMed: 12004111]

170. Le TT, Rehrer CW, Huff TB, Nichols MB, Camarillo IG, Cheng JX. Nonlinear optical imaging to evaluate the impact of obesity on mammary gland and tumor stroma. Mol Imaging. 2007; 6:205–211. [PubMed: 17532886]
171. Brown E, McKee T, Tomaso E, Pluen A, Seed B, Boucher Y, Jain RK. Dynamic imaging of collagen and its modulation in tumors in vivo using second-harmonic generation. Nat Med. 2003; 9:796–800. [PubMed: 12754503]
172. Han X, Burke RM, Zettel ML, Tang P, Brown EB. Second harmonic properties of tumor collagen: determining the structural relationship between reactive stroma and healthy stroma. Opt Express. 2008; 16:1846–1859. [PubMed: 18542263]
173. Preul MC, Caramanos Z, Collins DL, Villemure JG, Leblanc R, Olivier A, Pokrupa R, Arnold DL. Accurate, noninvasive diagnosis of human brain tumors by using proton magnetic resonance spectroscopy. Nat Med. 1996; 2:323–325. [PubMed: 8612232]
174. Hakumäki JM, Kauppinen RA. 1H NMR visible lipids in the life and death of cells. Trends Biochem Sci. 2000; 25:357–362. [PubMed: 10916153]
175. Caoili EM, Korobkin M, Francis IR, Cohan RH, Platt JF, Dunnick NR, Raghupathi KI. Adrenal masses: Characterization with combined unenhanced and delayed enhanced CT. Radiology. 2002; 222:629–633. [PubMed: 11867777]
176. Barba I, Cabanas ME, Arus C. The Relationship between Nuclear Magnetic Resonance-Visible Lipids, Lipid Droplets, and Cell Proliferation in Cultured C6 Cells. Cancer Res. 1999; 59:1861–1868. [PubMed: 10213493]
177. Le TT, Huff TB, Cheng JX. Coherent anti-Stokes Raman scattering imaging of lipids in cancer metastasis. BMC Cancer. 2009; 9:42. [PubMed: 19183472]
178. Fuchs E. Keratins and the skin. Annu Rev Cell Dev Biol. 1995; 11:123–153. [PubMed: 8689554]
179. Zimmerley M, McClure RA, Choi B, Potma EO. Following dimethyl sulfoxide skin optical clearing dynamics with quantitative nonlinear multimodal microscopy. Appl Optics. 2009; 48:D79–D87.
180. Lin JY, Fisher DE. Melanocyte biology and skin pigmentation. Nature. 2007; 445:843–850. [PubMed: 17314970]
181. Conovaloff A, Wang HW, Cheng JX, Panitch A. Imaging growth of neurites in conditioned hydrogel by coherent anti-stokes raman scattering microscopy. Organogenesis. 2009; 5:149–155. [PubMed: 20357972]
182. Brackmann C, Bodin A, Akeson M, Gatenholm P, Enejder A. Visualization of the Cellulose Biosynthesis and Cell Integration into Cellulose Scaffolds. Biomacromolecules. 2010; 11:542–548. [PubMed: 20158282]
183. Herrera S. Bonkers about biofuels. Nat Biotechnol. 2006; 24:755–760. [PubMed: 16841053]
184. Uhrich KE, Cannizzaro SM, Langer RS, Shakesheff KM. Polymeric systems for controlled drug release. Chem Rev. 1999; 99:3181–3198. [PubMed: 11749514]
185. Kang E, Robinson J, Park K, Cheng JX. Paclitaxel distribution in poly(ethylene glycol)/poly(lactide-co-glycolic acid) blends and its release visualized by coherent anti-Stokes Raman scattering microscopy. J Control Release. 2007; 122:261–268. [PubMed: 17574291]
186. Kang E, Wang H, Kwon IK, Song YH, Kamath K, Miller KM, Barry J, Cheng JX, Park K. Application of coherent anti-Stokes Raman scattering microscopy to image the changes in a paclitaxel-poly(styrene-b-isobutylene-b-styrene) matrix pre- and post-drug elution. J Biomed Mater Res A. 2008; 87A:913–920. [PubMed: 18228250]
187. Kang EN, Wang HF, Kwon IK, Robinson J, Park K, Cheng JX. In situ visualization of paclitaxel distribution and release by coherent anti-stokes Raman scattering microscopy. Anal Chem. 2006; 78:8036–8043. [PubMed: 17134137]
188. Windbergs M, Jurna M, Offerhaus HL, Herek JL, Kleinebudde P, Strachan CJ. Chemical Imaging of Oral Solid Dosage Forms and Changes upon Dissolution Using Coherent Anti-Stokes Raman Scattering Microscopy. Anal Chem. 2009; 81:2085–2091. [PubMed: 19209888]
189. Kam NWS, O'Connell M, Wisdom JA, Dai HJ. Carbon nanotubes as multifunctional biological transporters and near-infrared agents for selective cancer cell destruction. Proc Natl Acad Sci USA. 2005; 102:11600–11605. [PubMed: 16087878]

190. Barone PW, Baik S, Heller DA, Strano MS. Near-infrared Optical Sensors Based on Single-Walled Carbon Nanotubes. Nat Mater. 2005; 4:86–92. [PubMed: 15592477]

191. Liu Z, Tabakman S, Welsher K, Dai H. Carbon Nanotubes in Biology and Medicine: In Vitro and In Vivo Detection, Imaging and Drug Delivery. Nano Res. 2009; 2:85–120. [PubMed: 20174481]

192. Welsher K, Liu Z, Daranciang D, Dai H. Selective Probing and Imaging of Cells with Single Walled Carbon Nanotubes as Near-Infrared Fluorescent Molecules. Nano Lett. 2008; 8:586–590. [PubMed: 18197719]

193. Tong L, Wei QS, Wei A, Cheng JX. Gold Nanorods as Contrast Agents for Biological Imaging: Optical Properties, Surface Conjugation and Photothermal Effects. Photochem Photobiol. 2009; 85:21–32. [PubMed: 19161395]

194. Gindy ME, Prud'homme RK. Multifunctional nanoparticles for imaging, delivery and targeting in cancer therapy. Expert Opin Drug Deliv. 2009; 6:865–878. [PubMed: 19637974]

195. Giljohann DA, Seferos DS, Daniel WL, Massich MD, Patel PC, Mirkin CA. Gold Nanoparticles for Biology and Medicine. Angew Chem Int Ed. 2010; 49:3280–3294.

196. Danckwerts M, Novotny L. Optical frequency mixing at coupled gold nanoparticles. Phys Rev Lett. 2007; 98

197. Heller D, Baik S, Eurell T, Strano M. Single-Walled Carbon Nanotube Spectroscopy in Live Cells: Towards Long-Term Labels and Optical Sensors. Adv Mater. 2005; 17:2793–2799.

198. Liu Z, Li X, Tabakman SM, Jiang K, Fan S, Dai H. Multiplexed Multicolor Raman Imaging of Live Cells with Isotopically Modified Single Walled Carbon Nanotubes. J Am Chem Soc. 2008; 130:13540–13541. [PubMed: 18803379]

199. Zavaleta C, de la Zerda A, Liu Z, Keren S, Cheng Z, Schipper M, Chen X, Dai H, Gambhir SS. Noninvasive Raman Spectroscopy in Living Mice for Evaluation of Tumor Targeting with Carbon Nanotubes. Nano Lett. 2008; 8:2800–2805. [PubMed: 18683988]

200. De La Zerda A, Zavaleta C, Keren S, Vaithilingam S, Bodapati S, Liu Z, Levi J, Smith BR, Ma TJ, Oralkan O, Cheng Z, Chen X, Dai H, Khuri-Yakub BT, Gambhir SS. Carbon nanotubes as photoacoustic molecular imaging agents in living mice. Nat Nano. 2008; 3:557–562.

201. Fu Y, Huff TB, Wang HW, Wang HF, Cheng JX. *Ex vivo* and *in vivo* imaging of myelin fibers in mouse brain by coherent anti-Stokes Raman microscopy. Opt Express. 2008; 16:19396–19409. [PubMed: 19030027]

202. Henry FP, Cote D, Randolph MA, Rust EAZ, Redmond RW, Kochevar IE, Lin CP, Winograd JM. Real-Time In Vivo Assessment of the Nerve Microenvironment with Coherent Anti-Stokes Raman Scattering Microscopy. Plast Reconstr Surg. 2009; 123:123s–130s. [PubMed: 19182671]

203. Kennedy AP, Sutcliffe J, Cheng JX. Molecular composition and orientation of myelin figures characterized by coherent anti-Stokes Raman scattering microscopy. Langmuir. 2005; 21:6478–6486. [PubMed: 15982056]

204. Potma EO, Xie XS. Detection of single lipid bilayers with coherent anti-Stokes Raman scattering (CARS) microscopy. J Raman Spectrosc. 2003; 34:642–650.

205. Munhoz F, Rigneault H, Brasselet S. High Order Symmetry Structural Properties of Vibrational Resonances Using Multiple-Field Polarization Coherent Anti-Stokes Raman Spectroscopy Microscopy. Phys Rev Lett. 2010; 105:123903. [PubMed: 20867642]

206. Wang H, Huff TB, Fu Y, Jia KY, Cheng JX. Increasing the imaging depth of coherent anti-Stokes Raman scattering microscopy with a miniature microscope objective. Opt Lett. 2007; 32:2212–2214. [PubMed: 17671587]

207. Balu M, Liu G, Chen Z, Tromberg BJ, Potma EO. Fiber delivered probe for efficient CARS imaging of tissues. Opt Express. 2010; 18:2380–2388. [PubMed: 20174068]

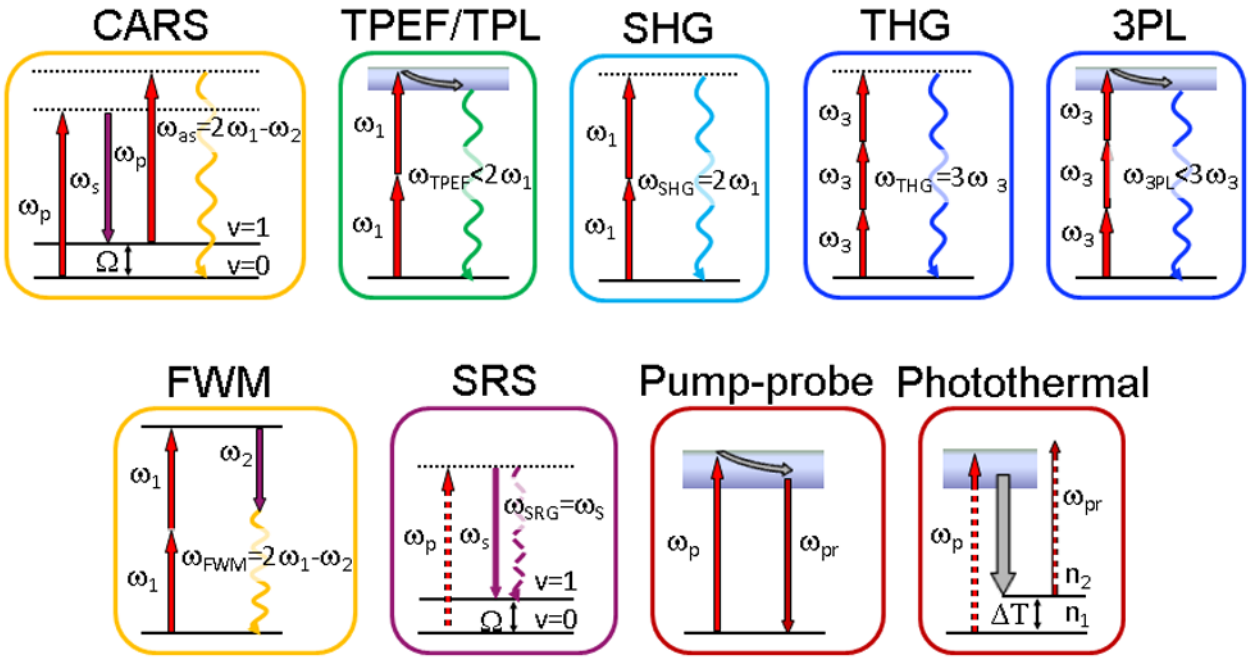

Figure 1.

Energy diagrams of NLO modalities. Solid lines represent electronic and vibrational states of molecules, dashed lines are virtual states. The straight arrows are excitation beams, the wavy arrows are output signal beams. The gray arrows represent relaxation in electronically excited states. ω_1 and ω_2 are two beams available in CARS microscope. $\omega_p = \omega_1$ and $\omega_s = \omega_2$ in CARS and SRS level diagram. Here SRG is shown as an example for SRS. $\omega_p = \omega_1$ and $\omega_{pr} = \omega_2$ in level diagrams for pump-probe and photothermal modalities. Ω is a frequency of vibrational transition between vibrational ground state v=0 and vibrationally excited state v=1. ω_1 and ω_2 are pump and Stokes beams from the laser sources, respectively. ω_3 is a long wavelength beam for THG and 3PL modalities available on optical parametric oscillator based laser systems for CARS microscope. ΔT is temperature change due to excitation. n_1 and n_2 are refractive indexes of material before and after excitation, respectively.

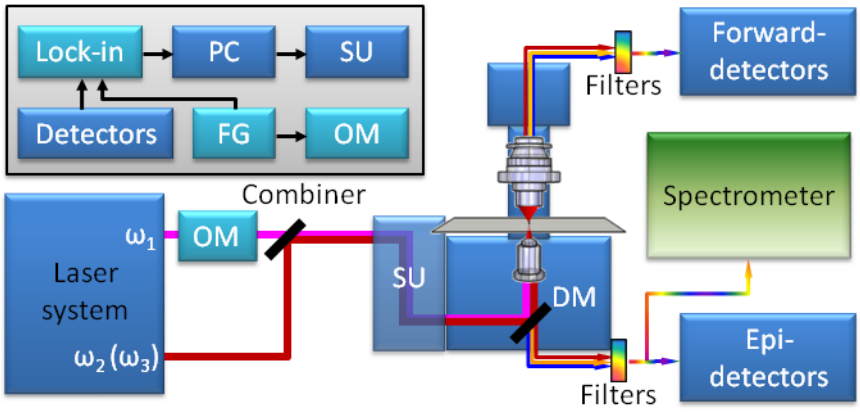

Figure 2.

Multimodal NLO microscope. ω_1 and ω_2 are pump and Stokes beams used for CARS and two-beam modalities, respectively. ω_3 is a longer wavelength (lower frequency) beam available in OPO based laser systems ($\omega_1 > \omega_2 > \omega_3$). OM is an optical modulator, SU is a scanning mirror unit. DM is an exchangeable dichroic mirror. The inset shows the connections between electronic components for phase sensitive heterodyne detection. Lock-in is a lock-in amplifier, PD is a photodiode, PC is a computer, FG is a function generator. The blue colored components are used for modalities with homodyne type of detection. The light blue color represents components required for modalities with heterodyne detection. The spectrometer is a part of compound Raman modality.

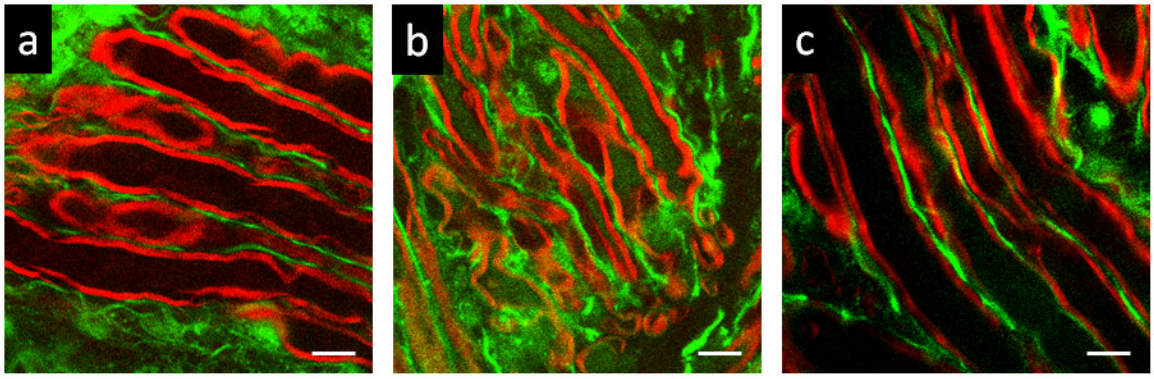

Figure 3.

CARS/TPEF imaging reveals calcium influx into myelinated axons (red: CARS, green: TPEF). TPEF images of Oregon Green 488 (green) and CARS images of myelin (red) show intraaxonal free Ca^{2+} levels in compression-injured (**b**), healthy (**a**), and micelle-treated (**c**) spinal cords. Images were acquired 1 h after compression injury. 0.67 mg/ml micelles were added immediately after compression injury. Scalar bars = 10 μm. Images adapted from reference [122].

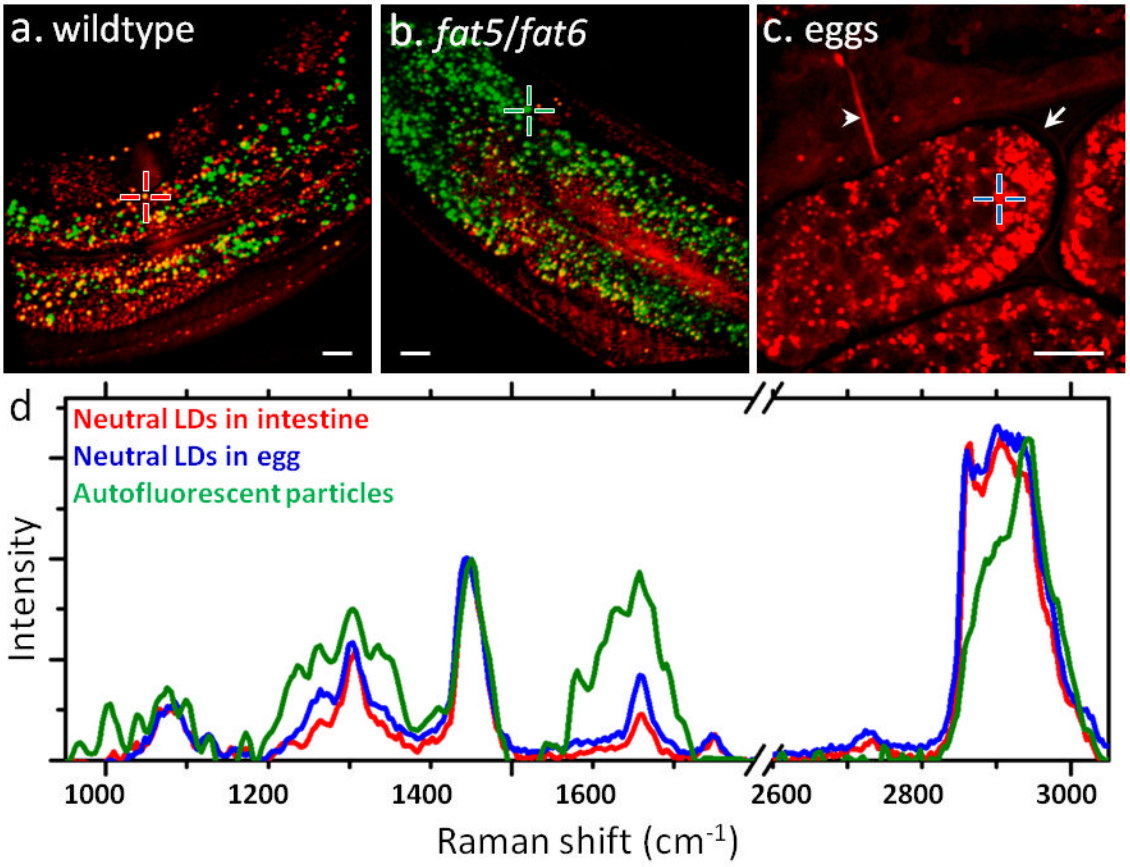

Figure 4.

CARS/TPEF imaging and confocal Raman spectral analysis of lipids in *C. elegans* (red: CARS, green: TPEF). (**a–b**) Overlaid CARS and TPEF images of neutral lipids (red) and autofluorescent particles (green) in a wildtype (**a**) and a *fat-5/fat-6* double mutant (**b**) *C. elegans*. The *fat-5/fat-6* double mutant has genetic deletions of palmitoyl-CoA desaturase *fat-5* and stearoyl-CoA desaturases *fat-6.* (**c**) CARS image of eggs laid outside of an adult *C. elegans*. Arrow: eggshell. Arrowhead: vulva. (**d**) Overlaid Raman spectra of neutral LDs in intestine (red line, corresponding to the red cross in **a**), neutral LDs in eggs (blue line, corresponding to the blue cross in **c**), and autofluorescent particles (green line, corresponding to the green cross in **b**). Scalar bars = 10 μm. Images in **a–b** are adapted from reference [109].

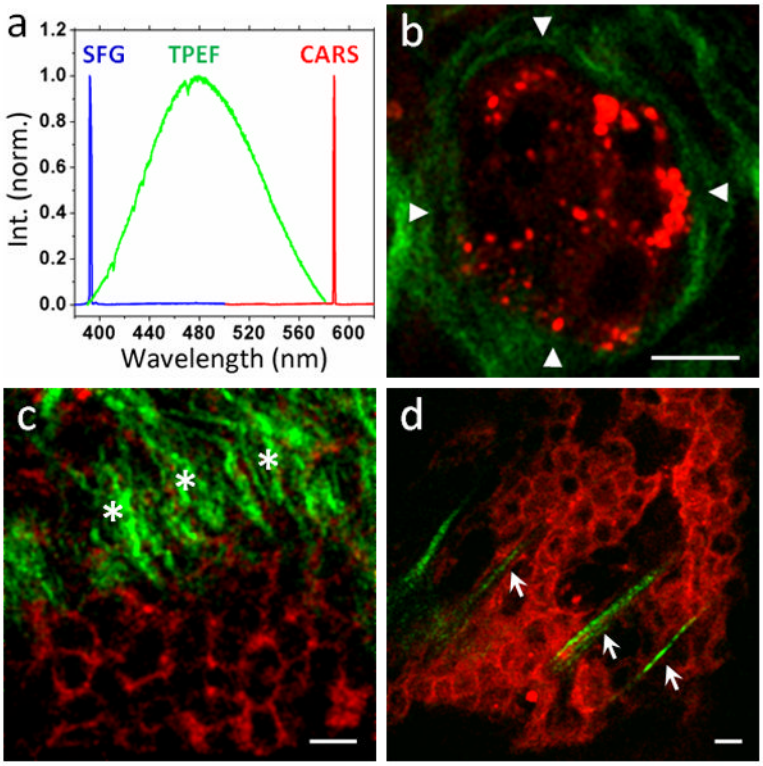

Figure 5.

CARS/SFG imaging distinguishes mammary adenoma and adenocarcinoma (red: CARS, green: SFG). (**a**) Emission spectra of SFG signals from collagen fibrils (blue), TPEF signals from Hoechst 33342-labeled nuclei (green), and CARS signals from lipid droplets (red). (**b**) CARS/SFG images of rat mammary adenoma. Abundant wavy collagen type I fibrils (green) form a smooth organized outer contour (arrow heads) to concentrically wrap around the localized tumor mass (red), whose signals come from lipid-rich cell membranes and lipid droplets. (**c–d**) CARS/SFG images of rat mammary adenocarcinoma. Straight collagen type I fibrils (green) were observed either perpendicularly against (**c**, asterisks) or within (**d**, arrows) or the tumor mass (red). Scalar bars = 10 μm.

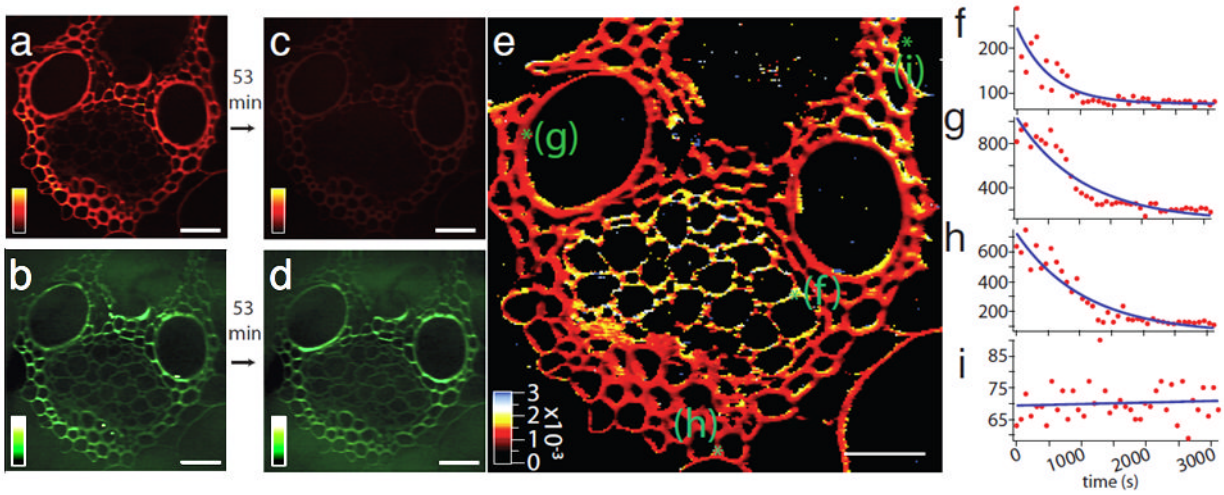

Figure 6.

Real-time SRS imaging of a delignification reaction in corn stover. (**a**) Lignin signal at 1600 cm^{-1} before the start of the reaction. (**b**) The cellulose signal at 1100 cm^{-1} before the start of the reaction. (**c**) Lignin signal after a 53 min time course of acid chlorite treatment, showing significant reduction compared to (**a**). (**d**) Cellulose signal after treatment, which remains roughly the same as in (**b**). (**e**) False-color heat map of the reaction rate constant obtained by fitting the time series of the lignin decay in the reaction to a single exponential. The initial and final points are shown in images (**a**) and (**c**). The rate-constant [s^{-1}] color scale is shown in the bottom left corner. (**f–i**) Representative time traces (red dots) and single exponential fits (blue lines) from four locations labeled as green spots in (**e**), representing a phloem element (**f**), vessel (**g**), fiber (**h**), and background with no plant cell wall (**i**) in the corn stover sample. The image in part (**e**) consists of 256×256 pixels, each of which has an associated single exponential decay fit to obtain the rate constant. Acquisition time: about 8 s/frame; spatial resolution: 900 nm (limited by the sampling of the images). Scalar bars = 40 μm. Images adapted from reference [60].

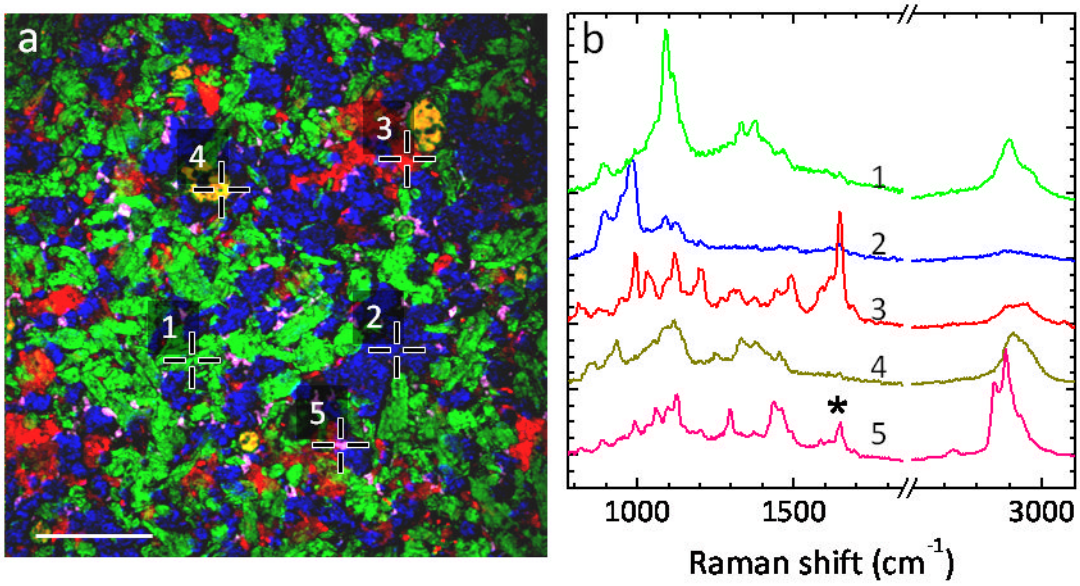

Figure 7.

SRS imaging and confocal Raman analysis of Pfizer tablet. (**a**) SRS image of API and excipients within the tablet Pfizer. The API is amlodipine besylate (AB), and the excipients consist of microcrystalline cellulose (MCC), dibasic calcium phosphate anhydrous (DCPA), sodium starch glycolate (SSG) and magnesium stearate (MS). The positions 1–5 correspond to MCC (green), DCPA (blue), AB (red), SSG (dark yellow) and MS (magenta), respectively. Scalar bar = 100 μm. (**b**) Raman spectra at the positions 1–5, respectively. Due to the large depth of field, the confocal Raman spectra show some contribution of Raman peaks from different components. For example, the spectrum 5 here is very similar to spectrum of pure MS, but has a contribution from spectrum of AB as indicated by asterisk. Images adapted from reference [59].

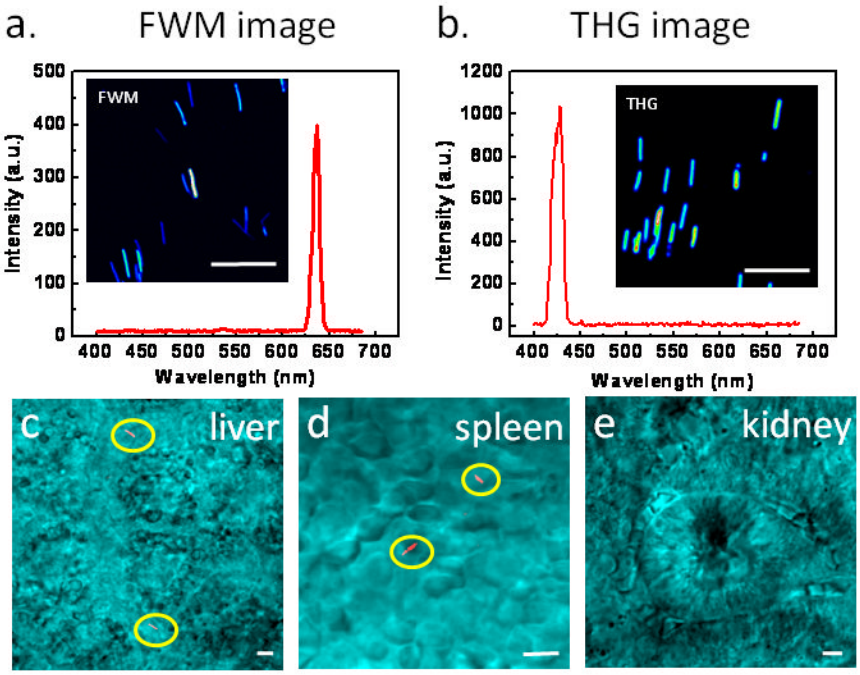

Figure 8.

SiNW as a NLO imaging agent. (**a**) FWM image and spectrum of SiNWs. The pump (790 nm) and Stokes (1018 nm) laser power at the sample were 0.8 and 1.2 mW, respectively. (**b**) THG image and spectrum of SiNWs. The 1290 nm laser power at the sample was 8.6 mW. (**c–e**) FWM images of SiNWs (red) deposited in liver (**c**), spleen (**d**), and kidney (**e**) explanted at 1 h post injection. FWM images in **c–e** are superimposed with transmission images (cyan) taken simultaneously. The SiNWs were highlighted by yellow circles. Scale bars = 5 μm. Images adapted from reference [52].